

The first- and second-order magneto-optical effects and intrinsically anomalous transport in 2D van der Waals layered magnets CrXY ($X = \text{S, Se, Te}$; $Y = \text{Cl, Br, I}$)

Xiuxian Yang,^{1,2,3} Ping Yang,^{1,2} Xiaodong Zhou,^{1,2} Wanxiang Feng,^{1,2,*} and Yugui Yao^{1,2}

¹Centre for Quantum Physics, Key Laboratory of Advanced Optoelectronic Quantum Architecture and Measurement (MOE), School of Physics, Beijing Institute of Technology, Beijing, 100081, China

²Beijing Key Lab of Nanophotonics & Ultrafine Optoelectronic Systems, School of Physics, Beijing Institute of Technology, Beijing, 100081, China

³Kunming Institute of Physics, Kunming 650223, China

(Dated: August 10, 2022)

Recently, the two-dimensional magnetic semiconductor CrSBr has attracted considerable attention due to its excellent air-stable property and high magnetic critical temperature. Here, we systematically investigate the electronic structure, magnetocrystalline anisotropy energy, first-order magneto-optical effects (Kerr and Faraday effects) and second-order magneto-optical effects (Schäfer-Hubert and Voigt effects) as well as intrinsically anomalous transport properties (anomalous Hall, anomalous Nernst, and anomalous thermal Hall effects) of two-dimensional van der Waals layered magnets CrXY ($X = \text{S, Se, Te}$; $Y = \text{Cl, Br, I}$) by using the first-principles calculations. Our results show that monolayer and bilayer CrXY ($X = \text{S, Se}$) are narrow band gap semiconductors, whereas monolayer and bilayer CrTeY are multi-band metals. The magnetic ground states of bilayer CrXY and the easy magnetization axis of monolayer and bilayer CrXY are confirmed by the magnetocrystalline anisotropy energy calculations. Utilizing magnetic group theory analysis, the first-order magneto-optical effects as well as anomalous Hall, anomalous Nernst, and anomalous thermal Hall effects are identified to exist in ferromagnetic state with out-of-plane magnetization. The second-order magneto-optical effects are not restricted by the above symmetry requirements, and therefore can arise in ferromagnetic and antiferromagnetic states with in-plane magnetization. The calculated results are compared with the available theoretical and experimental data of other two-dimensional magnets and some conventional ferromagnets. The present work reveals that monolayer and bilayer CrXY with superior magneto-optical responses and anomalous transport properties provide an excellent material platform for the promising applications of magneto-optical devices, spintronics, and spin caloritronics.

I. INTRODUCTION

According to the Mermin-Wagner theorem [1], the long-range magnetic order is strongly suppressed in low-dimensional systems mainly due to the enhanced thermal fluctuations, which makes the symmetry-breaking order unsustainable. Nevertheless, recent experimental fabrications of atomically-thin ferromagnetic (FM) CrI₃ [2] and Cr₂Ge₂Te₆ [3] films, which are mechanically exfoliated from their bulk van der Waals (vdW) materials, indicated that the long-range magnetic order can be established in two-dimensional (2D) systems in which the magnetic anisotropy plays a vital role. Since then, 2D magnetism has attracted enormous interest and more real materials were subsequently discovered, such as monolayer (ML) VSe₂ [4, 5], Fe₃GeTe₂ [6, 7], and CrTe₂ [8]. The ML VSe₂, Fe₃GeTe₂, and CrTe₂ are FM metals with relatively high Curie temperatures (T_C). The T_C of ML Fe₃GeTe₂ is around 130 K [6, 7], and the T_C of ML VSe₂ and CrTe₂ are even close to room-temperature [4, 5, 8], all of which are much larger than that of FM semiconductors CrI₃ ($T_C \sim 45$ K) [2] and Cr₂Ge₂Te₆ ($T_C \sim 25$ K) [3]. From the aspect of practical applications for 2D spintronics, it is imperative to search for magnetic semi-

conductors with higher T_C .

A vdW layered material, CrSBr, was synthesized fifty-years ago [9], and its bulk form has been identified to be an A-type antiferromagnetic (AFM) semiconductor with the Néel temperature (T_N) of 132 K and electronic band gap of ~ 1.5 eV [10, 11]. Recently, several theoretical works predicted that ML CrSBr is a FM semiconductor with high T_C ranging from 120 K to 300 K by different model calculations [12–18]. Bulk CrSBr can be mechanically exfoliated to ML and bilayer (BL), which were confirmed to be FM ($T_C \sim 146$ K) and AFM ($T_N \sim 140$ K), respectively, by a recent measurement of second harmonic generation [19]. The ML and BL CrSBr have been paid much attention because their magnetic critical temperatures are obviously higher than that of CrI₃ and Cr₂Ge₂Te₆. So far, some experimental works appear to focus on the fascinating properties of 2D CrSBr, including tunable magnetism [11, 19–23], magnon-exciton coupling [24], interlayer electronic coupling [20], tunable electronic transport [21], and etc. The AFM semiconductor CrSBr was also used to introduce magnetism in graphene/CrSBr heterostructure by considering the proximity effect [25]. However, the magnetotransport properties of 2D CrSBr, such as magneto-optical Kerr [26], Faraday [27], Schäfer-Hubert [28], and Voigt [29] effects (MOKE, MOFE, MOSHE, and MOVE) as well as anomalous Hall effect (AHE) [30], anomalous

* wxfeng@bit.edu.cn

Nernst effect (ANE) [31], and anomalous thermal Hall effect (ATHE) [32], remain largely unexplored. Since the family materials of CrXY ($X = \text{S, Se, Te; } Y = \text{Cl, Br, I}$) share the same crystal structure [15], atomically-thin films of CrXY should be easily obtained by the means of mechanical exfoliation, similarly to ML and BL CrSBr . A systematic study on the magneto-optical effects (including MOKE, MOFE, MOSHE, and MOVE) and intrinsically anomalous transport properties (including AHE, ANE, and ATHE) of ML and BL CrXY will contribute to further understanding of this class of 2D vdW magnets.

In this work, using the first-principles calculations, we systemically investigate the electronic, magnetic, optical, magneto-optical, and anomalous transport properties of ML and BL CrXY . We first reveal that CrSY and CrSeY are narrow band gap semiconductors, whereas CrTeY present multi-band metallic behaviors. Then, the magnetic ground state and the easy axis of magnetization for CrXY are confirmed by magnetocrystalline anisotropy energy (MAE) calculations. The results of MAE indicate that the easy axes of CrTeBr and CrTeI point along the out-of-plane direction (i.e., z -axis), while the other seven family members of CrXY prefer the in-plane magnetization. The BL CrSI , CrSeCl , and CrTeCl show strong interlayer FM coupling, whereas other six family members exhibit interlayer AFM coupling. Before calculating the magneto-optical and anomalous transport properties, we primarily analyze the shape of optical conductivity tensor by utilizing the magnetic group theory. The uncovered symmetry requirements indicate that the first-order magneto-optical effects (MOKE and MOFE) as well as the AHE, ANE, and ATHE can only arise in the FM state with out-of-plane magnetization. In order to explore the FM and AFM states with in-plane magnetization, we further study the second-order magneto-optical effects (MOSHE and MOVE). The calculated first- and second-order magneto-optical effects as well as intrinsically anomalous transport properties of CrXY are compared with other 2D magnets and some conventional ferromagnets. Our results show that 2D CrXY with superior magneto-optical responses and anomalous transport properties provide an excellent material platform for the promising applications of magneto-optical devices, spintronics, and spin caloritronics.

II. THEORY AND COMPUTATIONAL DETAILS

The magneto-optical effects, as a kind of fundamental magnetotransport phenomena in condensed matter physics, are usually considered to be a powerful probe of magnetism in low-dimensional systems [2, 3]. The MOKE and MOFE can be described as the rotation of the polarization planes of reflected and transmitted lights after a linearly polarized light hits on the surface of magnetic materials, respectively. Here, we only consider the MOKE and MOFE in the so-called polar geometry (e.g., both the directions of incident light and mag-

netization are along the z -axis), as shown in Fig. 1(a). The MOKE and MOFE are commonly regarded as first-order magneto-optical effects as their magnitudes are linearly proportional to the strength of magnetization and their signs are odd in the direction of magnetization. On the other hand, if the magnetization lies on the 2D atomic plane (i.e., xy -plane) and the angle between the electric field (\mathbf{E}) of incident light and the direction of magnetization (\mathbf{M}) is 45° , the polarization planes of reflected and transmitted lights still rotate, which are called MOSHE and MOVE [Fig. 1(b)], respectively. The MOSHE and MOVE are considered to be second-order magneto-optical effects as their magnitudes are quadratic to the strength of magnetization and their signs are even in the direction of magnetization.

It should be noted that in some FM and AFM materials, the first-order magneto-optical effects are prohibited due to the symmetry requirements, but the second-order magneto-optical effects can exist. Here, we take ML FM Fe_3GeTe_2 and BL AFM Fe_3GeTe_2 with in-plane magnetization [33] as examples to discuss this point. The magnetic point group of ML FM Fe_3GeTe_2 with in-plane magnetization (when the spin points to the x -axis) is $m'm'2'$, in which the mirror plane \mathcal{M}_x is perpendicular to the spin and is parallel to the z -axis. This mirror symmetry operation reverses the sign of the off-diagonal element of optical conductivity σ_{xy} ($\equiv \sigma^z$), thus indicating $\sigma_{xy} = 0$. If the spin points to the y -axis, the magnetic point group of ML FM Fe_3GeTe_2 is $m'm'2$, which contains a combined symmetry $\mathcal{T}\mathcal{M}_z$ (\mathcal{T} is the time-reversal symmetry, and \mathcal{M}_z is a mirror plane perpendicular to the z -axis and parallel to the spin). This combined symmetry operation reverses the sign of σ_{xy} , also suggesting $\sigma_{xy} = 0$. For BL AFM Fe_3GeTe_2 , the magnetic point groups are $2'/m$ and $2/m'$ when the spin points to the x - and y -axes, respectively. Both the two magnetic point groups have a combined symmetry \mathcal{TP} (\mathcal{T} and \mathcal{P} are the time-reversal and spatial inversion symmetries, respectively), which forces $\sigma_{xy} = 0$. Overall, in the cases of ML FM Fe_3GeTe_2 and BL AFM Fe_3GeTe_2 with in-plane magnetization, the vanishing off-diagonal element of optical conductivity ($\sigma_{xy} = 0$) can not give rise to the first-order magneto-optical effects (MOKE and MOFE), refer to Eqs. (1)–(3). In contrast, the second-order magneto-optical effects (MOSHE and MOVE) depend on both the off-diagonal and diagonal elements, see Eqs. (4)–(5). For the in-plane magnetization along either x - or y -axis, the two diagonal elements are not equivalent ($\sigma_{xx} \neq \sigma_{yy}$) due to the anisotropy of the in-plane optical response, which definitively induces the second-order magneto-optical effects regardless of whether the off-diagonal element is zero or not.

The Kerr and Faraday rotation angles (θ_K and θ_F), which are the deflection of the polarization plane with respect to the incident light, can be used to quantitatively characterize the magneto-optical performance. Additionally, the rotation angle $\theta_{K(F)}$ and ellipticity $\varepsilon_{K(F)}$ are usually combined into the complex Kerr (Faraday) an-

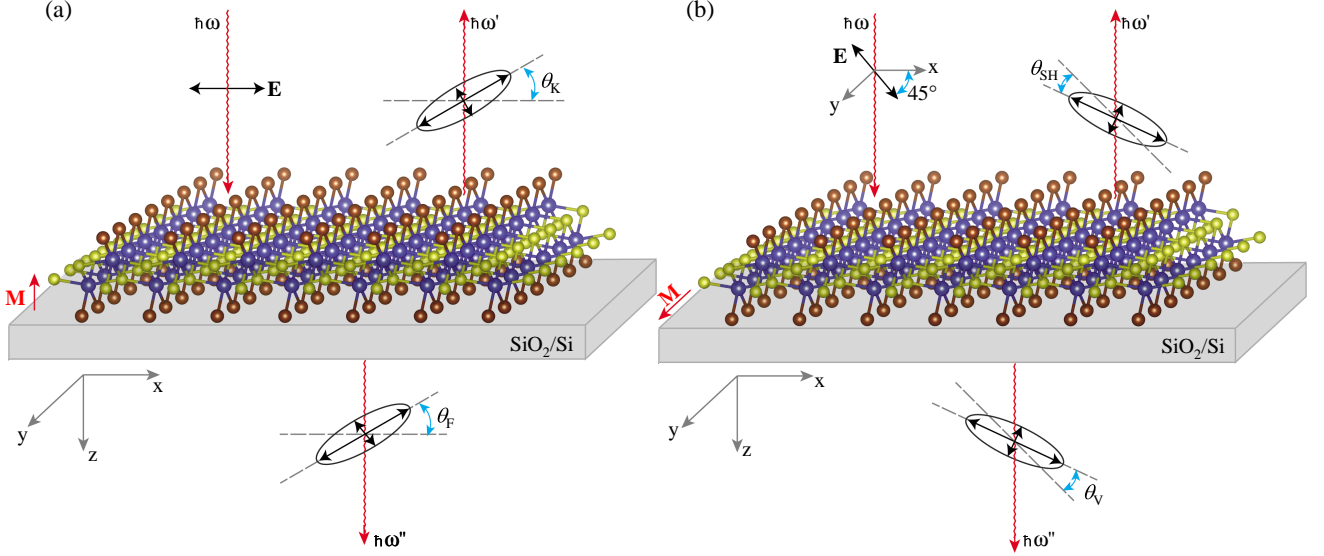


FIG. 1. (Color online) Schematic illustration of magneto-optical Kerr and Faraday effects (a) as well as magneto-optical Schäfer-Hubert and Voigt effects (b). $\hbar\omega$, $\hbar\omega'$, and $\hbar\omega''$ indicate the incident, reflected, and transmission lights, respectively. θ_K , θ_F , θ_{SH} , and θ_V represent the Kerr, Faraday, Schäfer-Hubert, and Voigt rotation angles, respectively. \mathbf{M} and \mathbf{E} label the magnetization and electric field of incident light, respectively. In (b), \mathbf{E} and \mathbf{M} form an angle of 45° on the xy plane.

gle [34–36],

$$\phi_K = \theta_K + i\varepsilon_K = i \frac{2\omega d}{c} \frac{\sigma_{xy}}{\sigma_{xx}^{\text{sub}}}, \quad (1)$$

and

$$\phi_F = \theta_F + i\varepsilon_F = \frac{\omega d}{2c} (n_+ - n_-), \quad (2)$$

$$n_{\pm}^2 = 1 + \frac{4\pi i}{\omega} (\sigma_0 \pm i\sigma_{xy}), \quad (3)$$

where c is the speed of light in vacuum, ω is frequency of incident light, d is the thickness of thin film, and n_{\pm} are the refractive indices for the right- and left-circularly polarized light, respectively. σ_{xx}^{sub} is the diagonal element of the optical conductivity tensor for a nonmagnetic substrate (e.g., SiO_2/Si , as shown in Fig. 1). In our calculations, only the interface between CrXY and SiO_2 layers is considered, and the SiO_2 layer is assumed to be thick enough. In this case, the Si layer is unimportant as it does not influence the magneto-optical properties of CrXY . The σ_{xx}^{sub} of the SiO_2 layer can be written as $i(1 - n_{\text{sub}}^2) \frac{\omega}{4\pi}$, here the n_{sub} is the energy-dependent refractive index of SiO_2 crystal (quartz) [37, 38]. σ_{xy} is the off-diagonal element of the optical conductivity tensor for a magnetic thin film and $\sigma_0 = \frac{1}{2}(\sigma_{xx} + \sigma_{yy})$ due to in-plane anisotropy.

In the case of MOSHE and MOVE, the rotation angle $\theta_{SH(V)}$ and ellipticity $\varepsilon_{SH(V)}$ can be also combined into the complex Schäfer-Hubert and Voigt angles. Considering the in-plane magnetization along the y -axis (Fig. 1),

the complex Schäfer-Hubert angle can be expressed as

$$\begin{aligned} \phi_{SH} &= \theta_{SH} + i\varepsilon_{SH} \\ &= \frac{-i\omega d}{c(1 - n_{\text{sub}}^2)} (n_{\parallel}^2 - n_{\perp}^2) \\ &= \frac{-i\omega d}{c(1 - n_{\text{sub}}^2)} [\epsilon_{yy} - \epsilon_{xx} - \frac{\epsilon_{zx}^2}{\epsilon_{zz}}], \end{aligned} \quad (4)$$

and the complex Voigt angle is give by [39, 40]

$$\begin{aligned} \phi_V &= \theta_V - i\varepsilon_V \\ &= \frac{\omega d}{2ic} (n_{\parallel} - n_{\perp}) \\ &= \frac{\omega d}{2ic} [\epsilon_{yy}^{\frac{1}{2}} - (\epsilon_{xx} + \frac{\epsilon_{zx}^2}{\epsilon_{zz}})^{\frac{1}{2}}]. \end{aligned} \quad (5)$$

Here, $\epsilon_{\alpha\beta} = \delta_{\alpha\beta} + \frac{4\pi i}{\omega} \sigma_{\alpha\beta}$ with $\alpha, \beta \in x, y, z$ is the permittivity tensor (in cgs units), n_{\parallel} and n_{\perp} are the refractive indices of a magnetic thin film that are parallel and perpendicular to the direction of magnetization, respectively.

From Eqs.(1)–(5), one would know that the key to calculate the first- and second-order magneto-optical effects is the optical conductivity, which can be obtained by the Kubo-Greenwood formula [41, 42],

$$\begin{aligned} \sigma_{xy} &= \sigma_{xy}^1(\omega) + i\sigma_{xy}^2(\omega) \\ &= \frac{ie^2\hbar}{N_k V} \sum_{\mathbf{k}} \sum_{n,m} \frac{f_{m\mathbf{k}} - f_{n\mathbf{k}}}{\varepsilon_{m\mathbf{k}} - \varepsilon_{n\mathbf{k}}} \\ &\quad \times \frac{\langle \psi_{n\mathbf{k}} | \hat{v}_x | \psi_{m\mathbf{k}} \rangle \langle \psi_{m\mathbf{k}} | \hat{v}_y | \psi_{n\mathbf{k}} \rangle}{\varepsilon_{m\mathbf{k}} - \varepsilon_{n\mathbf{k}} - (\hbar\omega + i\eta)}, \end{aligned} \quad (6)$$

where the superscripts 1 (2) indicates the real (imaginary) part of optical conductivity. $\psi_{n\mathbf{k}}$ and $\varepsilon_{n\mathbf{k}}$ are the Bloch function and interpolated energy at the band index n and momentum \mathbf{k} , respectively. $f_{n\mathbf{k}}$, V , N_k , $\hat{v}_{x(y)}$, $\hbar\omega$, and η are the Fermi-Dirac distribution function, volume of the unit cell, total number of k -points for sampling the Brillouin zone, the velocity operators, the photon energy, and energy smearing parameter, respectively. η was chosen to be 0.1 eV, corresponding to the carrier relaxation time of 6.5 fs, which is in the realistic range for multilayer transition metal chalcogenides [43, 44]. In this work, a sufficiently dense k -mesh of $450 \times 390 \times 1$ is used to calculate the optical conductivity. We also tested a denser k -mesh of $500 \times 430 \times 1$ for the convergence of optical conductivity, see Figs. S1(a) and S1(b) in Supplemental Material [45].

The AHE, which is featured by the transverse voltage drop induced by a longitudinal charge current in the absence of external magnetic field, is another fundamental magnetotransport phenomenon in condensed matter physics. The contributions to AHE can be distinguished to extrinsic (skew-scattering and side-jump) and intrinsic mechanisms [30]. The extrinsic AHE is dependent on the scattering of electrons off impurities or due to disorder, while the intrinsic AHE originates from the Berry phase nature of the electrons in a perfect crystal. In this work, we only focus on the intrinsically anomalous transport, i.e., intrinsic AHE. The first-order magneto-optical effects and intrinsic AHE share the similar physical origin, and the dc limit of the real part of the off-diagonal element of optical conductivity, $\sigma_{xy}^1(\omega \rightarrow 0)$, is nothing but the intrinsic anomalous Hall conductivity (AHC). Based on the linear response theory, the intrinsic AHC can be calculated [46],

$$\sigma_{xy} = -\frac{e^2\hbar}{V} \sum_{n,\mathbf{k}} f_{n\mathbf{k}} \Omega_{xy}^n(\mathbf{k}), \quad (7)$$

in which $f_{n\mathbf{k}}$ is the Fermi-Dirac distribution function, V is volume of the unit cell, and $\Omega_{xy}^n(\mathbf{k})$ is the band- and momentum-resolved Berry curvatures, given by

$$\Omega_{xy}^n(\mathbf{k}) = -\sum_{n' \neq n} \frac{2\text{Im}[\langle \psi_{n\mathbf{k}} | \hat{v}_x | \psi_{n'\mathbf{k}} \rangle \langle \psi_{n'\mathbf{k}} | \hat{v}_y | \psi_{n\mathbf{k}} \rangle]}{(\varepsilon_{n\mathbf{k}} - \varepsilon_{n'\mathbf{k}})^2}. \quad (8)$$

To calculate σ_{xy} , a k -mesh of $600 \times 520 \times 1$ was used. We also tested the convergence of σ_{xy} on a denser k -mesh of $750 \times 650 \times 1$, see supplemental Fig. S1(c) [45].

In addition to the AHE, the transverse charge current can also be induced by a longitudinal temperature gradient field, named ANE [31]. Additionally, a transverse thermal current arise under the longitudinal temperature gradient field, which is called ATHE or anomalous Righi-Leduc effect [32]. The magnetic materials that show large anomalous Nernst conductivity (ANC) and anomalous thermal Hall conductivity (ATHC) have great potentials to apply for spin caloritronics or thermoelectric devices. The AHE, ANE, and ATHE are closely related

to each other, and can be expressed through the anomalous transport coefficients in the generalized Landauer-Büttiker formalism [47–49],

$$R_{xy}^{(n)} = \int_{-\infty}^{\infty} dE (E - \mu)^n \left(-\frac{\partial f}{\partial E}\right) \sigma_{xy}(E), \quad (9)$$

where E , μ , and f are energy, chemical potential, and Fermi-Dirac distribution function, respectively. σ_{xy} is the intrinsic AHC calculated by Eq. (7) at zero temperature. Then, the temperature-dependent ANC (α_{xy}) and ATHC (κ_{xy}) are written as

$$\alpha_{xy} = -R_{xy}^{(1)}/eT, \quad (10)$$

$$\kappa_{xy} = R_{xy}^{(2)}/e^2T. \quad (11)$$

To calculate α_{xy} and κ_{xy} , the integral in Eq. (9) is set in the range of [-1.0, 2.5] eV for semiconductors and [-1.0, 1.0] eV for metals, with the energy interval of 0.0001 eV.

The first-principles density functional theory calculations were performed by utilizing the Vienna *ab initio* simulation package (VASP) [50, 51]. The projector augmented wave (PAW) method [52] was used and the generalized gradient approximation (GGA) with the Perdew-Burke-Ernzerhof parameterization [53] was adopted to treat the exchange-correlation functional. Dispersion correction was performed at the van der Waals density functional (vdW-DF) level [54–56], where the optB86b functional was used for the exchange potential. For the ML and BL structures, the vacuum layer with a thickness of at least 15 Å was used to avoid the interactions between adjacent layers. All structures were fully relaxed until the force on each atom was less than $0.001 \text{ eV} \cdot \text{Å}^{-1}$. To describe the strong correlation effect of the d orbitals on Cr atom, the GGA+U method [57] was used by taking appropriate parameters of U and J in the range of 4.05 ~ 4.40 eV and 0.80 ~ 0.97 eV [15], respectively. The values of U and J used for each compound are listed in supplemental Tab. S1 [45]. To obtain accurate MAE, a large plane-wave cutoff energy of 600 eV and a Monkhorst-Pack k -mesh of $15 \times 13 \times 1$ were used. The spin-orbit coupling (SOC) was included in the calculations of MAE, magneto-optical effects, and anomalous transport properties. The maximally localized Wannier functions were constructed by WANNIER90 package [41], and the d , p , and p orbitals of Cr, X ($X = \text{S, Se, Te}$), and Y ($Y = \text{Cl, Br, I}$) atoms were projected onto the Wannier functions, respectively. Totally, there are 44 and 88 Wannier functions for ML and BL CrXY, respectively, which converged adequately the results of magneto-optical effects and anomalous transport properties. Similarly, the computational technique employing the maximally localized Wannier functions can be in principle used to calculate the physical quantities that are closely related to orbital angular momenta [58–61]. The ISOTROPY software [62] was used to identify magnetic space and point groups. The workflow of the various codes used in our work is depicted in supplemental Fig. S2 [45].

III. RESULTS AND DISCUSSION

A. Crystal, magnetic, and electronic structures

Figure 2 shows the crystal structure of vdW layered materials CrXY ($X = \text{S, Se, Te}$; $Y = \text{Cl, Br, I}$). One can see that CrXY has a rectangular 2D primitive cell, in which a ML is made of two buckled planes of CrX sandwiched by two Y sheets, and a BL is formed by two MLs with the AA stacking order referring to experimental works [11, 19, 20, 63]. The relaxed lattice constants of ML and BL structures are collected in supplemental Tab. S1 [45]. The calculated lattice constants of ML CrSBr, $a = 3.54 \text{ \AA}$, $b = 4.79 \text{ \AA}$, and thickness $d = 8.00 \text{ \AA}$, are in good agreement with the experimental results, $a = 3.50 \text{ \AA}$, $b = 4.76 \text{ \AA}$ [11], and $d = 7.8 \pm 0.3 \text{ \AA}$ [19].

The magnetic anisotropy plays a vital role in stabilizing the long-range magnetic order of 2D systems. The MAE is defined as the difference of total energies between different magnetization directions (such as, along the x -, y -, and z -axis), which can be directly obtained by the first-principles calculations. To determine the magnetic ground states, we calculate the MAE of ML and BL CrXY. Since the FM ground state of ML CrXY was predicted by a recent theoretical work [15] and has been confirmed by two experimental works [19, 20], here we directly adopt the FM configuration as the ground state of ML CrXY. Thus, the magnetic ground states for ML CrXY can also be determined by the Goodenough-Kanamori rules, i.e., superexchange mechanism [64–66]. The magnetic exchange interactions can be judged by the angle of the chemical bonds connecting the ligand and two nearest-neighboring magnetic atoms. Particularly, a system prefers to be ferromagnetic if the angle equals 90° . Taking ML CrSBr as an example, the bond angle of Cr-Br-Cr is 88.96° , and the bond angles of Cr-S-Cr are 94.24° and 96.58° , suggesting the ferromagnetic ground state. Our calculated MAE indicate that ML CrSI, CrSeY prefer to the in-plane magnetization along the x -axis, ML CrSCl, CrSBr, and CrTeCl are in favor of in-plane magnetization along the y -axis, while ML CrTeBr and CrTeI take for the out-of-plane z -axis magnetization. The evolution of the easy axis from in-plane to out-of-plane direction can be explained by the SOC strength of the systems. The atomic SOC strength increases gradually in the consequences of $\text{S} \rightarrow \text{Se} \rightarrow \text{Te}$ and $\text{Cl} \rightarrow \text{Br} \rightarrow \text{I}$, and CrTeBr and CrTeI have the almost largest SOC strength among the other family compounds. It leads to the MAE results that CrTeBr and CrTeI have the out-of-plane z -axis magnetization, while the other family compounds have the in-plane x - or y -axis magnetization. This is similar to the case of 2D magnetic materials CrX_3 ($X = \text{Cl, Br, I}$) [67], in which the magnetization direction changes from in-plane (CrCl_3) to out-of-plane (CrI_3) with the increasing of SOC strength. For the BL CrXY, we compare the total energy of FM and AFM states (see supplemental Fig. S3 [45]), and find

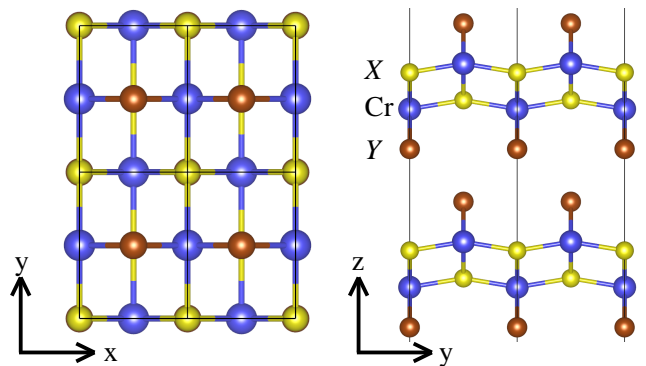


FIG. 2. (Color online) Top and side views of layered CrXY ($X = \text{S, Se, Te}$; $Y = \text{Cl, Br, I}$). The blue, yellow, and brown spheres represent Cr, X, and Y atoms, respectively. The black solid lines draw out the primitive cell. The experimental stacking order of bilayer structure is adopted.

that CrSI, CrSeCl, and CrTeCl exhibit the FM ground state, while the other six family members prefer to be AFM state. The easy magnetization axes of BL CrXY are identical to that of ML CrXY. The above results are summarized in supplemental Tab. S1 [45]. The easy magnetization axis of CrSBr is along the y -axis, which is in an accordance with the experimental reports [11, 19, 20].

After obtaining the magnetic ground states of CrXY, we shall further ascertain the corresponding magnetic groups as the group theory is a powerful tool to figure out the symmetry requirements for the magneto-optical effects and anomalous transport properties. The off-diagonal elements of optical conductivity tensor $[\sigma_{\alpha\beta}(\omega)]$ fully determine the symmetry requirements of first-order magneto-optical effects [see Eqs. (1)–(3)]. At zero frequency limit, $\sigma_{\alpha\beta}(\omega \rightarrow 0)$ is nothing but the intrinsic AHC [i.e., Eq. (7)], and therefore the symmetry requirements of AHE, ANE, and ATHE [refer to Eqs. (9)–(11)] should be the same as that of $\sigma_{\alpha\beta}(\omega)$. Here, we only need to analyze the symmetry results of $\sigma_{\alpha\beta}(\omega)$ under relevant magnetic groups.

Since the off-diagonal elements of optical conductivity tensor can be regarded as a pseudovector (like spin), its vector-form notation, $\boldsymbol{\sigma} = [\sigma^x, \sigma^y, \sigma^z] = [\sigma_{yz}, \sigma_{zx}, \sigma_{xy}]$, is used here for convenience. In 2D systems, only σ^z ($\equiv \sigma_{xy}$) is potentially nonzero, while σ^x ($\equiv \sigma_{yz}$) and σ^y ($\equiv \sigma_{zx}$) are always zero. It can be easily understood from Eq. (6) as the zero velocity along the z -axis (i.e., $\hat{v}_z = 0$, meaning that the electrons can not move along the out-of-plane direction in 2D systems) definitely gives rise to vanishing σ_{yz} and σ_{zx} . For ML and BL FM CrXY with any magnetization directions (x -, y -, or z -axis), the magnetic space and point groups of are always identified to be $Pm'm'n$ and $m'm'm$ [$D_{2h}(C_{2h})$ in Schönflies notation], respectively. It is sufficient for us to analyze magnetic point group due to the translationally invariance of σ_{xy} [68]. Hence, we only discuss the magnetic point group of $m'm'm$, in which there are one mirror

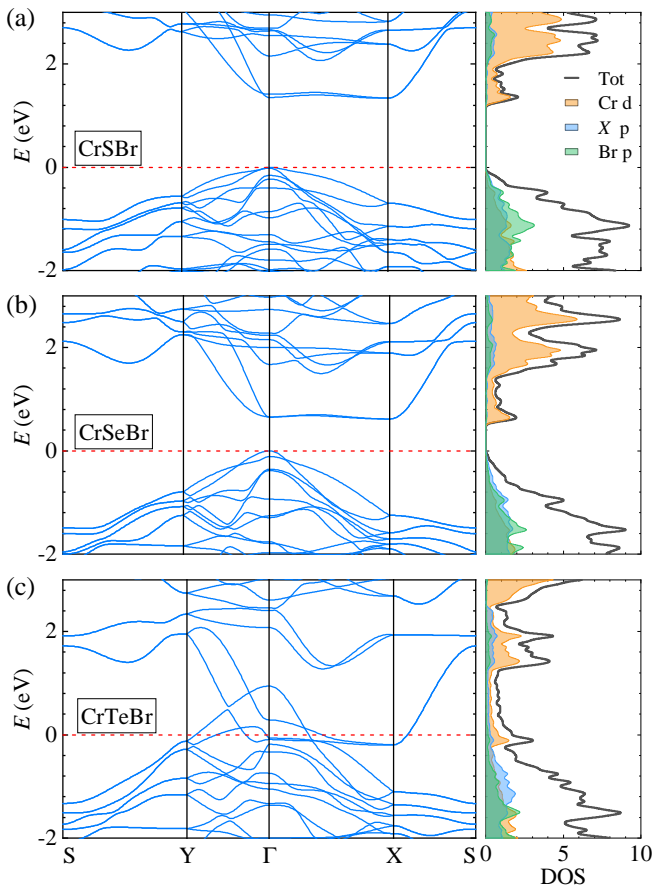


FIG. 3. (Color online) The relativistic band structures and orbital-decomposed density of states (in unit of states/eV per cell) for monolayer ferromagnetic $\text{Cr}X\text{Br}$ ($X = \text{S}, \text{Se}, \text{Te}$) with out-of-plane magnetization.

plane \mathcal{M} and two combined symmetries \mathcal{TM} (\mathcal{T} is the time-reversal symmetry). For the in-plane magnetization along the x -axis (y -axis), the mirror plane is \mathcal{M}_x (\mathcal{M}_y), which is perpendicular to the spin magnetic moment, such a mirror operation reverses the sign of σ_{xy} , indicating that σ_{xy} should be zero. On the other hand, for out-of-plane magnetization, the mirror plane is \mathcal{M}_z and two combined symmetries are \mathcal{TM}_x and \mathcal{TM}_y . The spin magnetic moment is perpendicular to the \mathcal{M}_z , which does not change the sign of σ_{xy} . Moreover, the mirror planes \mathcal{M}_x and \mathcal{M}_y are parallel to the spin, and both \mathcal{TM}_x and \mathcal{TM}_y preserve the sign of σ_{xy} . A conclusion here is that σ_{xy} is nonzero (zero) for ML and BL FM $\text{Cr}XY$ with out-of-plane (in-plane) magnetization. In the case of the BL AFM $\text{Cr}XY$, the magnetic space and point groups are $Pm'm'n'$ and $m'm'm'$ [$D_{2h}(D_2)$ in Schönflies notation] for out-of-plane magnetization, and are $Pm'mn$ and mmm' [$D_{2h}(C_{2v})$ in Schönflies notation] for in-plane magnetization. There is a combined symmetry \mathcal{TP} (\mathcal{P} is the spatial inversion) in the two point groups of $m'm'm'$ and mmm' , which forces σ_{xy} to be zero. Overall, a nonzero σ_{xy} can only exist in ML and BL

FM $\text{Cr}XY$ with out-of-plane magnetization, which turn out to be our target systems for studying the MOKE, MOFE as well as AHE, ANE, and ATHE. It should be noted that the out-of-plane magnetization is not the magnetic ground states for some family members of $\text{Cr}XY$, however, an applied external magnetic field can easily tune the spin direction, as already realized in layered CrSBr [20].

The first-order magneto-optical effects (MOKE and MOFE) can not exist in FM and AFM $\text{Cr}XY$ with in-plane magnetization, but it is not the case for the second-order magneto-optical effects (MOSHE and MOVE). According to the Onsager relations, the diagonal elements of the permittivity tensor are even in magnetization (\mathbf{M}), e.g., $\epsilon_{yy}(-\mathbf{M}) = \epsilon_{yy}(\mathbf{M})$. Furthermore, equations (4) and (5) show that the complex Schäfer-Hubert and Voigt angles depend on square of ϵ_{zx} . Therefore, the MOSHE and MOVE must be even in \mathbf{M} . In the case of FM and AFM $\text{Cr}XY$ with in-plane magnetization, although ϵ_{zx} is always zero, the MOSHE and MOVE do exist because of the nonvanishing ϵ_{yy} and ϵ_{xx} (the relation of $\epsilon_{yy} \neq \epsilon_{xx}$ also satisfies). Owing to this, we use the MOSHE and MOVE to characterize the in-plane magnetized ML FM and BL FM/AFM $\text{Cr}XY$. The complex Schäfer-Hubert and Voigt angles are calculated by orienting the spins along the y -axis, and the results of x -axis in-plane magnetization can be simply obtained by putting a minus sign, refer to Eqs. (4) and (5).

The relativistic band structures of ML FM and BL FM/AFM $\text{Cr}XY$ with out-of-plane and in-plane magnetization are plotted in supplemental Figs. S4–S9 [45]. The results show that CrSY and CrSeY are narrow band gap semiconductors, while CrTeY are multi-band metals. All the band gaps of CrSY and CrSeY are summarized in supplemental Tab. S1 [45]. Here, we choose ML FM $\text{Cr}X\text{Br}$ ($X = \text{S}, \text{Se}, \text{Te}$) as representative examples to discuss the electronic properties of $\text{Cr}XY$ family materials, as shown in Fig. 3. A clear trend can be seen that the band gaps of $\text{Cr}X\text{Br}$ become smaller and eventually disappear with the increasing of atomic number (e.g., $\text{S} \rightarrow \text{Se} \rightarrow \text{Te}$). The orbital-decomposed density of states of ML FM $\text{Cr}X\text{Br}$ show that the d orbitals of Cr atom and p orbitals of X and Br atoms are dominant components near the Fermi level. For CrSBr , the calculated band gaps of ML FM, BL FM, and BL AFM states are 1.34 eV, 1.22 eV, and 1.30 eV, respectively, which are in good agreement with that of bulk material (~ 1.25 eV) [11]. Since CrSY and CrSeY are narrow band gap semiconductors, the electrons and holes could bound in pairs to form quasiparticle excitons. Taking CrSBr as an example [20], the exciton binding energies for ML FM, BL FM, and BL AFM states are 0.5 eV, 0.37 eV, and 0.46 eV, respectively, which are apparently smaller than the exciton binding energies of ML FM CrI_3 (1.7 eV [69], 1.06 eV [70], and 0.84 [70]). It indicates that the relatively weak excitonic effects in CrSY and CrSeY may not significantly influence the optical and magneto-optical properties, in contrast to CrI_3 [69, 70].

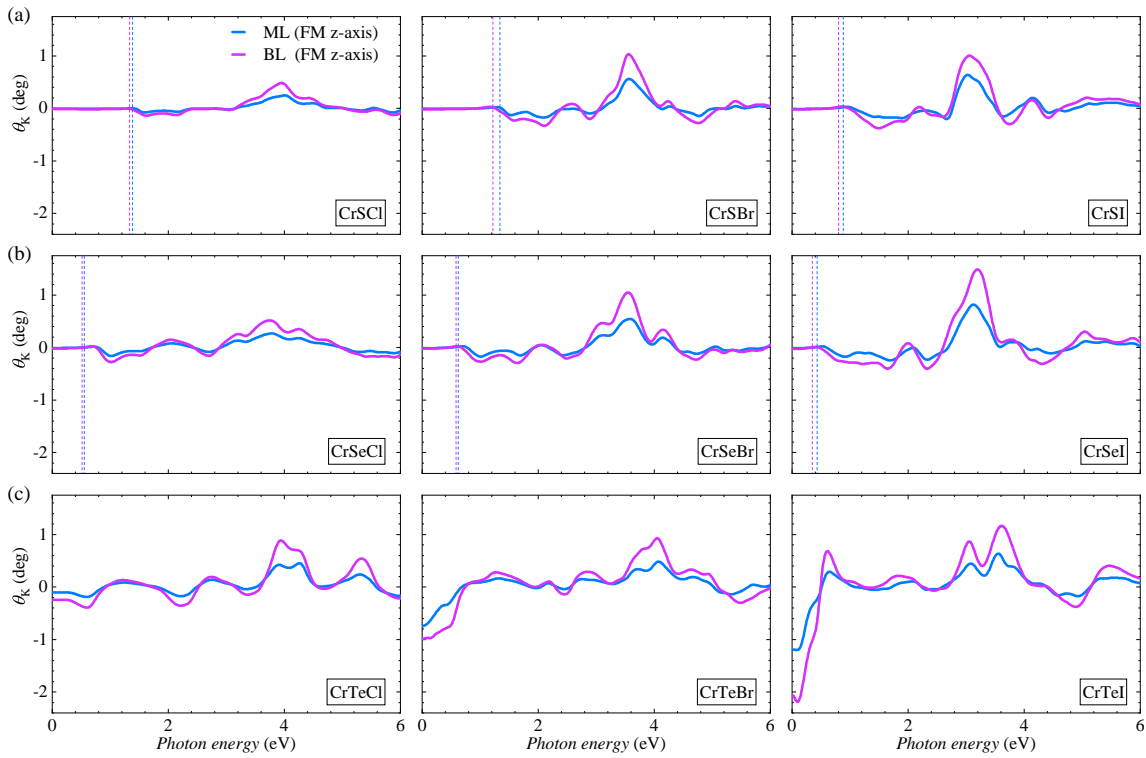


FIG. 4. (Color online) The magneto-optical Kerr rotation angles (θ_K) of monolayer (blue solid lines) and bilayer (pink solid lines) ferromagnetic CrXY ($X = \text{S, Se, Te}$; $Y = \text{Cl, Br, I}$) with out-of-plane magnetization. The vertical dashed lines in (a) and (b) indicate the band gaps.

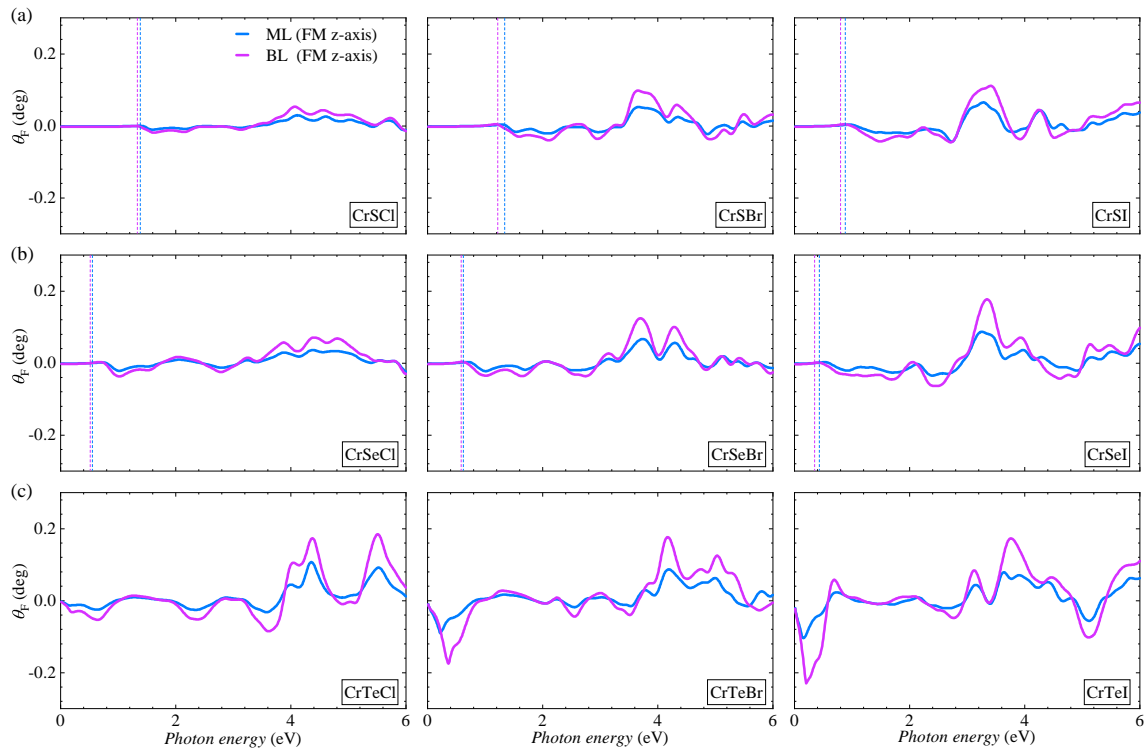


FIG. 5. (Color online) The magneto-optical Faraday rotation angles (θ_F) of monolayer (blue solid lines) and bilayer (pink solid lines) ferromagnetic CrXY ($X = \text{S, Se, Te}$; $Y = \text{Cl, Br, I}$) with out-of-plane magnetization. The vertical dashed lines in (a) and (b) indicate the band gaps.

TABLE I. The maximums of Kerr, Faraday, Schäfer-Hubert, and Voigt rotation angles (θ_K , θ_F , θ_{SH} , and θ_V) in the moderate energy range (1 ~ 5 eV) as well as the corresponding incident photon energy ($\hbar\omega$) for monolayer and bilayer CrXY. Here, θ_K and θ_F are calculated under the ferromagnetic states with out-of-plane magnetization, while θ_{SH} and θ_V are calculated under ferromagnetic or antiferromagnetic states with in-plane y -axis magnetization. For a better comparison, θ_F and θ_V are given in two units, deg and deg/ μm (in the parentheses), which can be converted to each other by considering the effective thickness of crystal structures along the z -axis.

		θ_K (deg)	$\hbar\omega$ (eV)	θ_F (deg) (deg/ μm)	$\hbar\omega$ (eV)	θ_{SH} (deg)	$\hbar\omega$ (eV)	θ_V (deg) (deg/ μm)	$\hbar\omega$ (eV)
CrScI	ML (FM)	0.25	4.01	0.04 (54.29)	4.11	-4.65	3.65	0.41 (559.34)	3.69
	BL (FM)	0.48	3.95	0.06 (33.93)	4.07	-9.30	3.66	0.85 (579.39)	3.70
	BL (AFM)					-8.64	3.66	0.76 (513.05)	3.70
CrSBr	ML (FM)	0.56	3.56	0.06 (75.02)	3.66	-3.92	3.10	0.40 (496.28)	3.13
	BL (FM)	1.04	3.56	0.11 (68.76)	3.65	6.01	3.69	-0.80 (-502.03)	2.66
	BL (AFM)					9.87	2.24	-0.77 (-478.74)	2.28
CrSI	ML (FM)	0.64	3.02	0.08 (90.60)	3.28	5.90	3.30	-0.55 (-624.74)	3.37
	BL (FM)	1.00	3.06	0.12 (67.95)	3.41	8.63	3.37	-0.90 (-507.99)	3.41
	BL (AFM)					6.60	3.35	-0.77 (-436.75)	2.30
CrSeCl	ML (FM)	0.27	3.78	0.04 (49.52)	4.38	-3.66	3.40	0.31 (421.07)	4.76
	BL (FM)	0.51	3.74	0.08 (54.81)	4.41	6.99	2.82	-0.84 (-577.27)	2.91
	BL (AFM)					7.00	2.74	-0.76 (-524.16)	2.89
CrSeBr	ML (FM)	0.54	3.58	0.08 (101.94)	3.74	3.93	2.30	0.43 (552.31)	1.65
	BL (FM)	1.05	3.55	0.15 (95.57)	3.70	7.48	2.29	0.76 (484.44)	1.63
	BL (AFM)					10.27	2.45	0.87 (551.30)	1.63
CrSeI	ML (FM)	0.82	3.12	0.10 (114.72)	3.25	3.62	1.90	-0.44 (-504.61)	1.93
	BL (FM)	1.49	3.19	0.20 (114.72)	3.35	6.27	2.00	0.63 (362.78)	1.27
	BL (AFM)					5.17	1.92	-0.53 (-304.59)	1.99
CrTeCl	ML (FM)	0.45	4.26	0.10 (132.58)	4.36	8.54	2.66	-1.01 (-1342.27)	2.72
	BL (FM)	0.89	3.94	0.17 (114.92)	4.37	13.39	2.76	-1.67 (-1107.05)	2.85
	BL (AFM)					11.31	2.77	-1.50 (-994.53)	2.91
CrTeBr	ML (FM)	0.48	4.07	0.09 (110.91)	4.19	4.68	2.45	-0.57 (-731.54)	2.50
	BL (FM)	0.93	4.05	0.18 (112.56)	4.17	8.08	2.54	-1.07 (-680.64)	2.61
	BL (AFM)					10.15	2.66	-1.27 (-811.67)	2.70
CrTeI	ML (FM)	0.64	3.56	0.08 (93.56)	3.64	-2.53	4.28	0.32 (377.20)	4.48
	BL (FM)	1.17	3.61	0.19 (112.48)	3.76	-4.94	3.40	-0.46 (-269.45)	2.48
	BL (AFM)					-7.25	3.39	-0.66 (-388.03)	3.05

B. First-order magnetic-optical effects

The calculated optical conductivities (σ_{xx} , σ_{yy} , and σ_{xy}) for ML and BL FM CrXY with out-of-plane magnetization are displayed in supplemental Figs. S10–S13 [45]. The spectra of optical conductivity of ML and BL structures have similar shape due to the weak vdW interaction [73]. After obtaining the optical conductivity tensors, we can calculate the first-order magneto-optic effects, i.e., MOKE and MOFE, according to Eqs. (1)–(3). The Kerr and Faraday rotation angles (θ_K and θ_F) and the corresponding ellipticities (ε_K and ε_F) as a function of photon energy are illustrated in Figs. 4–5 and supplemental Figs. S14–S15 [45], respectively. From Figs. 4(a)–

4(b), one can observe that the θ_K of ML and BL CrSY and CrSeY are vanishing within the band gap due to the semiconducting nature, while increase largely in high energy region. The ML and BL CrTeY exhibit distinct θ_K from zero frequency, suggesting the metallic property, as displayed in Fig. 4(c). The same features can also be found in the Faraday rotation angles θ_F [see Fig. 5]. The resultant MOKE and MOFE are thus consistent with the above analysis about the electronic structures of CrXY.

Especially, the peaks of θ_K and θ_F for ML and BL CrXY appear at almost the same incident photon energy, as shown in Figs. 4 and 5. In the moderate energy range (1 ~ 5 eV), the θ_K and θ_F are remarkably large. Taking CrXBr as examples, the maximal values of θ_K

TABLE II. The magneto-optical Kerr, Faraday, Schäfer-Hubert, and Voigt rotation angles (θ_K , θ_F , θ_{SH} , and θ_V) for CrXY and other 2D magnetic materials. For a better comparison, the absolute values of rotation angles are used here as the sign only indicates the rotation direction with respect to the principle axis of incident light that may have different definitions in literatures. Moreover, the rotation angles are given in a range due to the dependence on the number of layers for some 2D materials. The data marked by "Exp" are experimental measurements, while the others are computational results.

	θ_K (deg)	θ_F (deg/ μm)	θ_{SH} (deg)	θ_V (deg)
CrXY	0.25~1.49	33.93~132.58	2.53~13.39	0.31~1.67
CrI ₃	0.29~2.86 [2] ^{Exp} 0.60~1.30 [71]	50~108 [71]		
CrTe ₂	0.24~1.76 [72]	30~173 [72]		
CrGeTe ₃	0.0007~0.002 [3] ^{Exp} 0.9~2.2 [73]	100~120 [73]		
GA	0.13~0.81 [74]	9.3~137.8 [74]		
BP	0.02~0.12 [74]	1.4~18.9 [74]		
InS	0.34 [75]	84.3 [75]		
Fe _n GeTe ₂ ($n = 3, 4, 5$)	0.74~2.07 [33]	50.28 ~ 222.66 [33]		
CoO			0.007 [76] ^{Exp}	
CuMnAs				0.023 [77] ^{Exp}

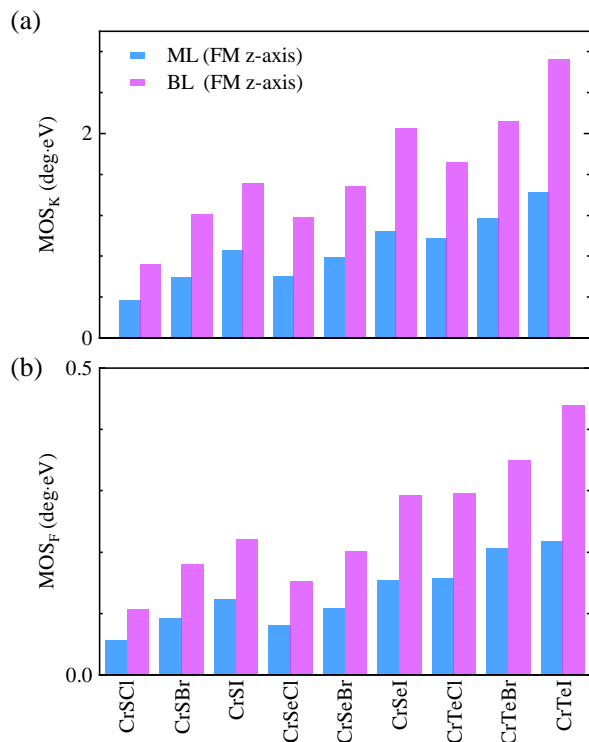


FIG. 6. (Color online) The magneto-optical strength of Kerr (a) and Faraday (b) effects for monolayer and bilayer CrXY with out-of-plane magnetization.

(θ_F) for ML CrXBr ($X = \text{S, Se, Te}$) are 0.56° (0.06°), 0.54° (0.08°), and 0.48° (0.09°), respectively. And the maximal values of θ_K (θ_F) for BL CrXBr ($X = \text{S, Se,$

Te) are 1.04° (0.11°), 1.05° (0.15°), and 0.93° (0.18°), respectively. The maximal values of θ_K and θ_F as well as the corresponding photon energies for ML and BL CrXY are summarized in Tab. I. The Kerr rotation angles θ_K of ML and BL CrXY are comparable or even larger than that of conventional ferromagnets and some famous 2D ferromagnets, e.g., bcc Fe (-0.5° [35]), hcp Co (-0.42°) [78], fcc Ni (-0.25°) [79], CrI₃ (ML 0.29° , trilayer 2.86°) [2], CrTe₂ (ML 0.24° , trilayer -1.76°) [72], CrGeTe₃ (BL 0.0007° , trilayer 0.002°) [3], gray arsenene (ML 0.81° , BL-AA 0.13° , BL-AC 0.14° , here AA and AC are stacking patterns.) [74], blue phosphorene (ML 0.12° , BL-AA 0.02° , BL-AB 0.03° , BL-AC 0.03°) [74], InS (ML 0.34°) [75], and Fe_nGeTe₂ ($n = 3, 4, 5$) ($0.74^\circ \sim 2.07^\circ$) [33]. In addition, the Faraday rotation angles θ_F of ML and BL CrXY are also comparable or larger than that of some famous 2D ferromagnets, such as CrI₃ (ML $50^\circ/\mu\text{m}$, BL $75^\circ/\mu\text{m}$, trilayer $108^\circ/\mu\text{m}$) [71], CrTe₂ (ML $30 \sim -173^\circ/\mu\text{m}$) [72], CrGeTe₃ (ML $120^\circ/\mu\text{m}$, trilayer $100^\circ/\mu\text{m}$) [73], gray arsenene (ML $137.8^\circ/\mu\text{m}$, BL-AA $9.3^\circ/\mu\text{m}$, BL-AC $10.0^\circ/\mu\text{m}$) [74], blue phosphorene (ML $18.9^\circ/\mu\text{m}$, BL-AA $1.4^\circ/\mu\text{m}$, BL-AB $2.3^\circ/\mu\text{m}$, BL-AC $2.2^\circ/\mu\text{m}$) [74], InS ($84.3^\circ/\mu\text{m}$) [75], and Fe_nGeTe₂ ($n = 3, 4, 5$) ($50.28 \sim 222.66^\circ/\mu\text{m}$) [33]. The above magneto-optical data are summarized in Tab. II for a better comparison.

The Kerr and Faraday rotation angles (θ_K and θ_F) at a given photon energy are obviously increasing with the thin-film thickness of CrXY, which can be easily seen from Tab. I and Figs. 4 and 5. In order to quantitatively describe the overall trend of Kerr and Faraday spectra, we here introduce a physical quantity called magneto-

optical strengths (MOS) [75, 80, 81]

$$\begin{aligned} \text{MOS}_K &= \int_{0^+}^{\infty} \hbar |\theta_K(\omega)| d\omega, \\ \text{MOS}_F &= \int_{0^+}^{\infty} \hbar |\theta_F(\omega)| d\omega. \end{aligned} \quad (12)$$

MOS_K and MOS_F are plotted in Figs. 6(a) and 6(b), respectively, from which one can observe that the MOKE and MOFE of BL CrXY are nearly double that of ML CrXY. It is simply because that the MOKE and MOFE as the first-order magneto-optical effects are proportional to the magnetization, which is linearly dependent on the number of layers. This trend has also been observed in 2D van der Waals magnets CrI₃ [2] and Cr₂Ge₂Te₆ [73]. Moreover, a clear step-up trend of θ_K and θ_F can be seen in ML and BL CrXY by changing X (S \rightarrow Se \rightarrow Te) or Y (Cl \rightarrow Br \rightarrow I). It can be understood that the MOKE and MOFE are also proportional to the SOC strength, which increases with the atomic number. This trend can also be found in our previous work about hole-doped MX ($M = \text{Ga, In}$; $X = \text{S, Se, Te}$) monolayer, in which the MOKE and MOFE have a size consequence of $\text{In}X > \text{Ga}X$ due to the larger SOC strength of In atom.

C. Second-order magneto-optical effects

The first-order magneto-optical effects (MOKE and MOFE) are forbidden in ML and BL CrXY with in-plane magnetization, while the second-order magneto-optical effects (MOSHE and MOVE) can arise without the restriction by symmetry. Here, we illustrate the MOSHE and MOVE of ML FM and BL FM/AFM CrXY by taking the in-plane y -axis magnetization as an example, and the results of the x -axis magnetization can be obtained by putting a minus sign (refer to Eqs. (4) and (5) and note that ϵ_{zx} equals zero due to the symmetry restriction). It has to be mentioned here that due to the in-plane crystal anisotropy of CrXY (a 2D rectangular primitive cell), the natural linear birefringence exists. This phenomenon is actually not related to magnetism, and can not be mixed into the second-order magneto-optical effects [82]. The diagonal elements of permittivity tensor can be expanded into a Taylor series in powers of magnetization \mathbf{M} (up to second-order),

$$\epsilon_{\alpha\alpha}(\mathbf{M}) = \epsilon_{\alpha\alpha}^{(0)} + \epsilon_{\alpha\alpha}^{(1)}\mathbf{M} + \epsilon_{\alpha\alpha}^{(2)}\mathbf{M}^2, \quad (13)$$

where $\epsilon_{\alpha\alpha}^{(0)}$ is the part independent on magnetization, $\epsilon_{\alpha\alpha}^{(1)}$ and $\epsilon_{\alpha\alpha}^{(2)}$ are linearly and quadratically dependent on magnetization, respectively. According to the Onsager relation, $\epsilon_{\alpha\alpha}(-\mathbf{M}) = \epsilon_{\alpha\alpha}(\mathbf{M})$, we know $\epsilon_{\alpha\alpha}^{(1)} = 0$. It turns out to be clear that $\epsilon_{\alpha\alpha}^{(0)}$ is responsible for the natural linear birefringence originating from crystal anisotropy, and $\epsilon_{\alpha\alpha}^{(2)}$ is responsible for the MOSHE and MOVE originating from magnetism. We first calculate $\epsilon_{\alpha\alpha}^{(0)}$ in 2D nonmagnetic CrXY by forcing the magnetic moments to be zero

during self-consistent field calculation, and then calculate $\epsilon_{\alpha\alpha}$ (the sum of $\epsilon_{\alpha\alpha}^{(0)}$ and $\epsilon_{\alpha\alpha}^{(2)}$) in 2D magnetic CrXY. Finally, $\epsilon_{\alpha\alpha}^{(2)}$ can be simply obtained by subtracting $\epsilon_{\alpha\alpha}^{(0)}$ from $\epsilon_{\alpha\alpha}$. Thus, we take $\epsilon_{\alpha\alpha}^{(2)}$ instead of $\epsilon_{\alpha\alpha}$ into Eqs. (4) and (5). The corresponding optical conductivities $\sigma_{\alpha\alpha}^{(2)}$ are shown in supplemental Figs. S16 and S17 [45].

The calculated Schäfer-Hubert and Voigt rotation angles (θ_{SH} and θ_V) of CrXY are plotted in Figs. 7 and 8, and the corresponding ellipticities (ϵ_{SH} and ϵ_V) are plotted in supplemental Figs. S18 and S19 [45]. The spectra of θ_{SH} and θ_V for semiconducting CrSY and CrSeY are negligibly small in the low energy range far below the band gaps. However, in contrast to the Kerr and Faraday effects, θ_{SH} and θ_V take on finite values near the band edges [e.g., Figs. 7(a) and 8(a)]. The reason is that θ_{SH} and θ_V depend on the diagonal elements of optical conductivity, which are nonvanishing within the band gap (see Figs. S16 and S17 [45]). In the energy range larger than the band gaps, θ_{SH} and θ_V oscillate frequently, as shown in Figs. 7(a,b) and 8(a,b), respectively. For metallic CrTeY, the relatively larger θ_{SH} and θ_V can be found in Figs. 7(c) and 8(c), respectively. Taking CrSBr as an example, the maximal values of θ_{SH} for ML FM, BL FM, and BL AFM states are -3.92° , 6.01° , and 9.87° at the photon energies of 3.10 eV, 3.69 eV, and 2.24 eV, respectively; the maximal values of θ_V for ML FM, BL FM, and BL AFM states are 0.40° , -0.80° , and -0.77° at the photon energies of 3.13 eV, 2.66 eV, and 2.28 eV, respectively. The data of the largest θ_{SH} and θ_V as well as the related photon energies for all CrXY family members are summarized in Tab. I. The θ_{SH} and θ_V of CrXY are larger than that of some 2D AFMs, for example, 10 nm thick CoO thin-film ($\theta_{SH} \sim 0.007$ deg) [76] and 10 nm thick CuMnAs thin-film ($\theta_V \sim 0.023$ deg) [77].

From Eqs. (4) and (5), one can know that θ_{SH} , ϵ_{SH} , θ_V , and ϵ_V are dominated by the two diagonal elements of permittivity tensor (ϵ_{yy} and ϵ_{xx}) as the off-diagonal element (ϵ_{zx}) is restricted to be zero by symmetry. By plugging the optical conductivity ($\epsilon_{yy(xx)} = 1 + \frac{4\pi i}{\omega} \sigma_{yy(xx)}$) into Eq. (4), one shall find $\theta_{SH} \propto -\sigma_{\text{diff}}^1 = -\text{Re}(\sigma_{yy} - \sigma_{xx})$ and $\epsilon_{SH} \propto -\sigma_{\text{diff}}^2 = -\text{Im}(\sigma_{yy} - \sigma_{xx})$. Figure 9 plots the real (σ_{diff}^1) and imaginary (σ_{diff}^2) parts of the difference between the diagonal elements of optical conductivities (σ_{yy} and σ_{xx}) for ML FM, BL FM, and BL AFM CrSBr. One can clearly observe that the spectral structure of θ_{SH} is determined by σ_{diff}^1 only differing by an opposite sign, comparing the middle panel of Fig. 7(a) with Fig. 9(a). The spectral structure of ϵ_{SH} is thus determined by σ_{diff}^2 , comparing the middle panel of supplemental Fig. S18(a) [45] with Fig. 9(b). On the other hand, there is not such a clear relation between θ_V (ϵ_V) and σ_{diff}^1 (σ_{diff}^2) since equation (5) involves the square roots of ϵ_{yy} and ϵ_{xx} , though the spectral structures of θ_V (ϵ_V) and σ_{diff}^1 (σ_{diff}^2) seem to be similar somewhere.

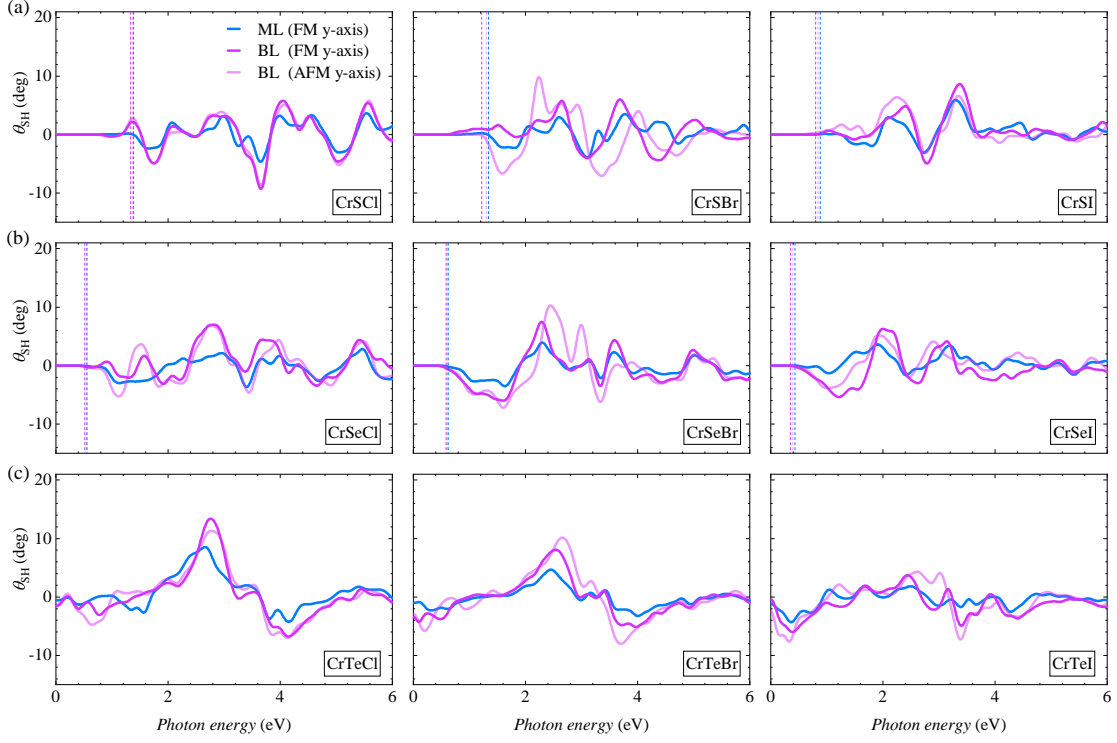


FIG. 7. (Color online) The magneto-optical Schärer-Hubert rotation angles (θ_{SH}) of monolayer ferromagnetic (blue solid lines), bilayer ferromagnetic (dark pink solid lines), and bilayer antiferromagnetic (light pink solid lines) CrXY with the in-plane magnetization along the y -axis. The vertical dashed lines in (a) and (b) indicate the band gaps.

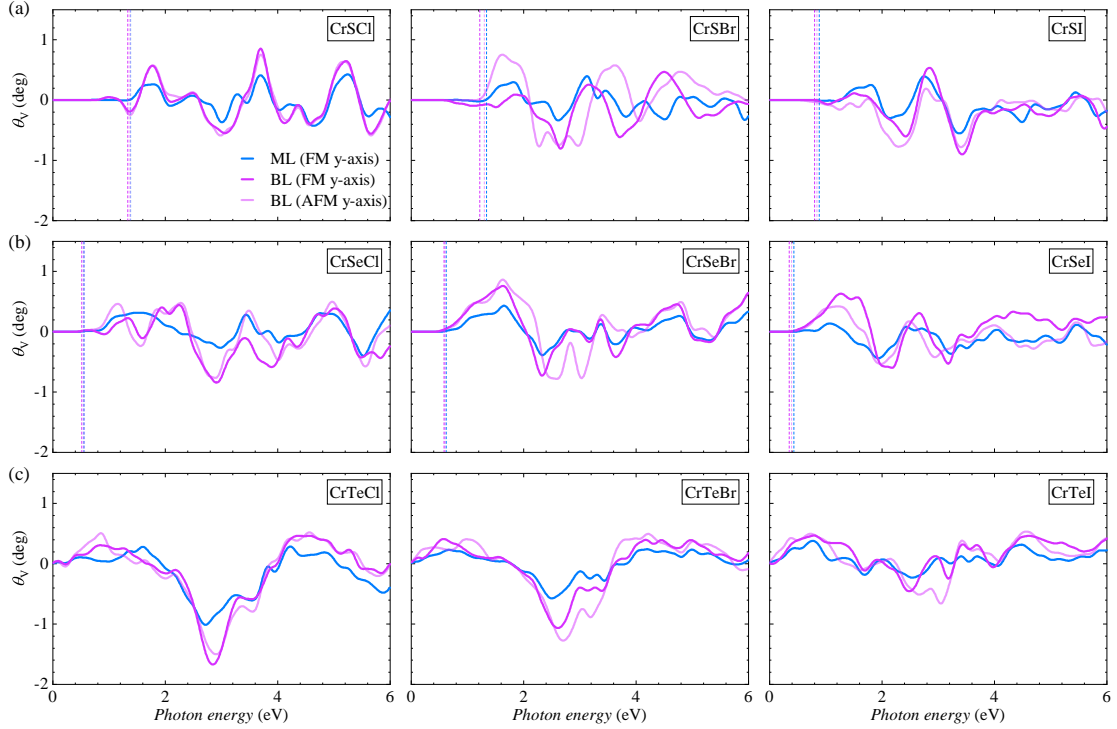


FIG. 8. (Color online) The magneto-optical Voigt rotation angles (θ_V) of monolayer ferromagnetic (blue solid lines), bilayer ferromagnetic (dark pink solid lines), and bilayer antiferromagnetic (light pink solid lines) CrXY with the in-plane magnetization along the y -axis. The vertical dashed lines in (a) and (b) indicate the band gaps.

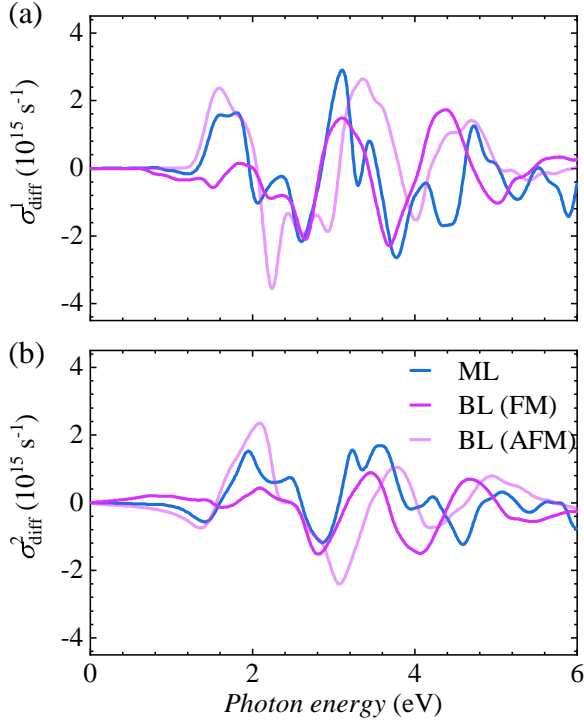


FIG. 9. (Color online) The real (a) and imaginary (b) parts of the difference between the two diagonal elements of optical conductivities ($\sigma_{\text{diff}} = \sigma_{yy} - \sigma_{xx}$) for monolayer ferromagnetic (blue solid lines), bilayer ferromagnetic (dark pink solid lines), and bilayer antiferromagnetic (light pink solid lines) CrSBr.

D. Anomalous Hall, anomalous Nernst, and anomalous thermal Hall effects

In this subsection, we shall discuss the AHE as well as its thermoelectric counterpart, ANE, and its thermal analogue, ATHE, for ML and BL FM CrXY with out-of-plane magnetization. The ANE and ATHE are evaluated at 100 K below the Curie temperatures by the theoretical prediction (> 108 K) [15] and experimental measurements (> 140 K) [19, 20]. The magnetic transition temperature can be in principle increased via doping effects. For example, magnetic atom-doped 2D transition metal dichalcogenides have been predicted to exhibit room-temperature ferromagnetism [83, 84]. Additionally, the Curie temperature of trilayer Fe_3GeTe_2 can be improved to room-temperature by ionic-liquid gating technique [7].

The calculated intrinsic AHC (σ_{xy}) as a function of energy are displayed in Fig. 10. For semiconducting CrSY and CrSeY, the AHC is zero within the band gaps, similarly to the magneto-optical Kerr and Faraday effects. For metallic CrTeY ($Y = \text{Cl}, \text{Br}, \text{I}$), σ_{xy} takes the values of $0.14 e^2/h$, $0.75 e^2/h$, and $1.05 e^2/h$ for ML FM states, and of $0.35 e^2/h$, $0.98 e^2/h$, and $1.56 e^2/h$ for BL FM states at the Fermi energy (E_F), respectively. The magnetotransport properties like the AHE can be

modulated by electron or hole doping, which shifts the E_F upward or downward, respectively. According to the recent experimental works [7, 85], the doping carrier concentration for 2D materials can reach up to 10^{15} cm^{-2} via the gate voltage. Then, the variation range of the E_F can be estimated in a reasonable range, see supplemental Fig. S20 [45], by taking ML CrXBr as examples. The energy ranges for ML and BL CrSY, CrSeY, and CrTeY are reasonably given to be $[-0.5, 2.0]$ eV, $[-0.5, 1.0]$, and $[-0.5, 0.5]$ eV, respectively. In the above energy regions, σ_{xy} increases up to $1.93 e^2/h$, $1.54 e^2/h$, and $1.57 e^2/h$ for ML CrSBr, CrTeCl, and CrTeBr at -0.40 eV, -0.39 eV, and -0.12 eV by hole doping, respectively. And σ_{xy} increases up to $2.12 e^2/h$, $1.88 e^2/h$, and $2.24 e^2/h$ for BL CrTeCl, CrTeBr, and CrTeI at -0.32 eV, -0.04 eV, and -0.16 eV by hole doping, respectively. On the other hand for electron doping, σ_{xy} can be reached to $1.60 e^2/h$, $2.12 e^2/h$, $3.61 e^2/h$ for BL CrTeCl, CrTeBr, and CrTeI at 0.23 eV, 0.14 eV, and 0.11 eV, respectively. It is obvious that the metallic CrTeY exhibit more prominent AHE than the semiconducting CrSY and CrSeY. The largest σ_{xy} for CrTeY are in the range of 544.46 – 827.95 S/cm (converted from the unit of e^2/h by considering the effective thickness), which is larger than bulk Fe_3GeTe_2 (140 – 540 S/cm) [86], thin film Fe_3GeTe_2 (~ 400 S/cm) [87], thin film Fe_4GeTe_2 (~ 180 S/cm) [88], and is even compared with bulk bcc Fe (751 S/cm [46], 1032 S/cm [89]).

Strikingly, a peak of σ_{xy} appears in BL CrSY and CrSeY near the bottom of conduction bands, and grows larger with the increasing of atomic number ($\text{Cl} \rightarrow \text{Br} \rightarrow \text{I}$), as displayed in Figs. 10(a) and 10(b). We interpret the underlying physical reasons by taking BL CrSeY as examples. At the energy position of the peaked σ_{xy} , there exists a band crossing in the band structure that is dominated by Cr $d_{x^2-y^2}$ orbitals [see the left inset in Fig. 10(b)]. The band crossing is a Weyl-like point, which is protected by the glide symmetry $\mathcal{M}_z \tau_{(\frac{1}{2}, \frac{1}{2}, 0)}$. It preserves even after including SOC because the glide symmetry still exists. Pinning the E_F at the band crossing point, the Berry curvature exhibits hot spots around the Γ point [see the right inset in Fig. 10(b)], which definitely gives rise to a large σ_{xy} . With the increasing of atomic number Y , the region of the hot spots of Berry curvature enlarges gradually, which enhances the peak of σ_{xy} .

The ANE, the thermoelectric counterpart of AHE, is a celebrated effect from the realm of the spin caloritronics [90, 91]. At the low temperature, the ANC (α_{xy}) is connected to the energy derivative of σ_{xy} via the Mott relation [92],

$$\alpha_{xy} = -\frac{\pi^2 k_B^2 T}{3e} \sigma'_{xy}(E), \quad (14)$$

which can be derived from Eq. (10). From the above equation, one can find that a steep slope of σ_{xy} versus energy generally leads to a large α_{xy} . For example, there appear two opposite peaks of α_{xy} close to the bottom of conduction bands for BL CrSY and CrSeY [see Figs. 11(a) and 11(b)], which exactly originates from the

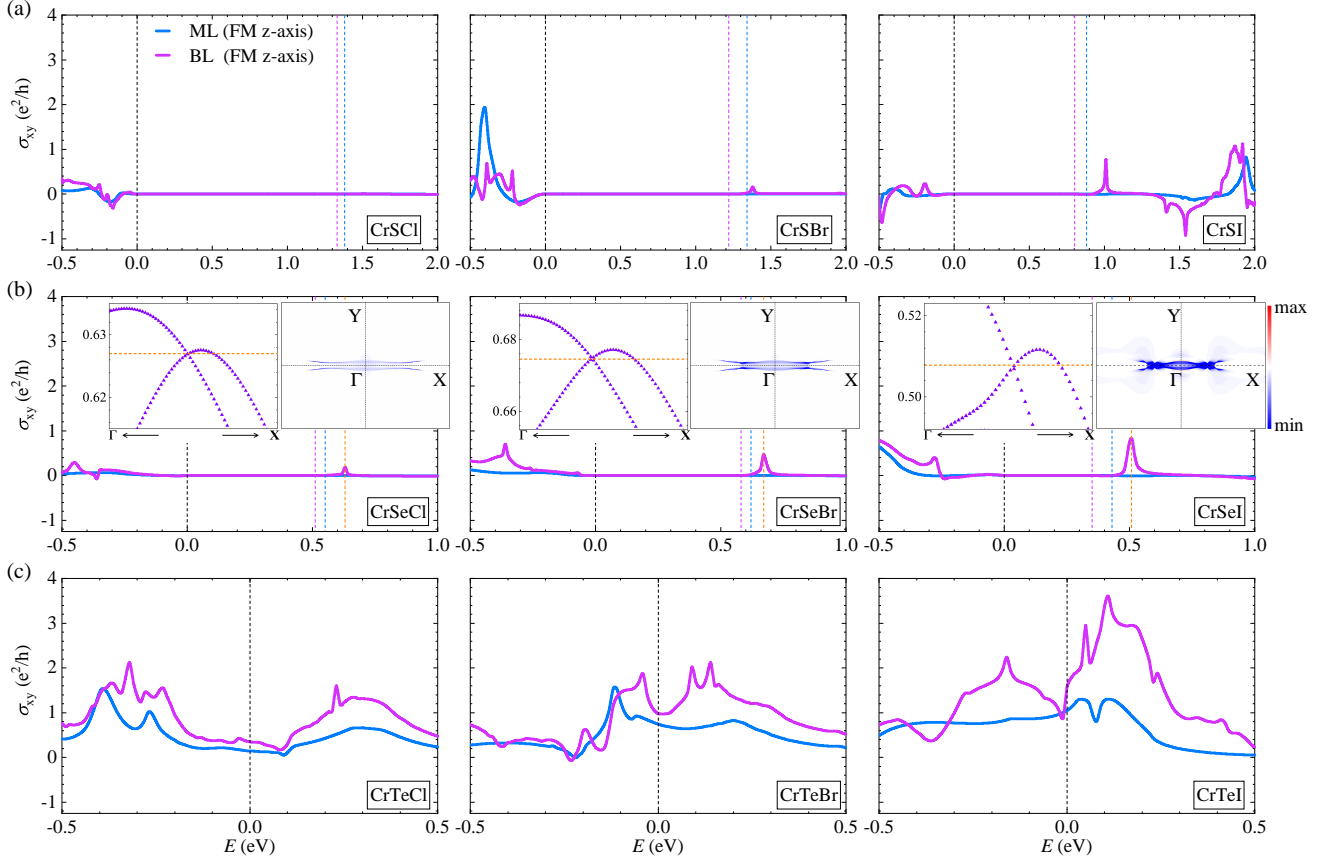


FIG. 10. (Color online) The intrinsic anomalous Hall conductivities (σ_{xy}) as a function of energy for monolayer (blue solid lines) and bilayer (pink solid lines) CrXY with out-of-plane magnetization. The black dashed lines indicate the true Fermi energy for metals or the top of valence bands for semiconductors. The blue and pink dashed lines indicate the bottom of conduction bands for monolayer and bilayer semiconducting CrSY/CrSeY, respectively. The right inset in (b) are momentum-resolved Berry curvature (in arbitrary unit) in 2D Brillouin zone. The left inset in (b) are orbital-projected band structures, in which the violet solid triangles present the components of Cr $d_{x^2-y^2}$ orbitals and the orange dashed lines label the energy position where the Berry curvature is calculated.

positive and negative slopes of the peak of σ_{xy} at the same energy [see Fig. 10(a) and (b)]. For semiconducting CrSY and CrSeY, α_{xy} is unsurprisingly zero within the electronic band gap. Among CrSY and CrSeY, ML CrSBr exhibits the excellent ANE under appropriate hole doping, such as $2.59 \text{ AK}^{-1}\text{m}^{-1}$ and $-3.71 \text{ AK}^{-1}\text{m}^{-1}$ at -0.38 eV and -0.44 eV , respectively. For metallic ML (BL) CrTeY with $Y = \text{Cl, Br, and I}$, the calculated α_{xy} at the true Fermi energy are 0.09 (0.09) $\text{AK}^{-1}\text{m}^{-1}$, 0.32 (0.36) $\text{AK}^{-1}\text{m}^{-1}$, and -0.58 (-1.13) $\text{AK}^{-1}\text{m}^{-1}$, respectively. By doping holes or electrons, α_{xy} can reach up to -2.13 (0.94) $\text{AK}^{-1}\text{m}^{-1}$ at -0.42 (-0.20) eV for ML (BL) CrTeCl, to -2.29 (-1.55) $\text{AK}^{-1}\text{m}^{-1}$ at -0.14 (-0.12) eV for ML (BL) CrTeBr, and to 0.90 (-1.29) $\text{AK}^{-1}\text{m}^{-1}$ at 0.16 (0.09) eV for ML (BL) CrTeI, respectively. The calculated $|\alpha_{xy}|$ of ML CrSBr, CrTeCl, and CrTeBr are considerably large ($> 2.0 \text{ AK}^{-1}\text{m}^{-1}$), which exceeds to bulk ferromagnets $\text{Co}_3\text{Sn}_2\text{S}_2$ ($\sim 2.0 \text{ AK}^{-1}\text{m}^{-1}$) [93] and Ti_2MnAl ($\sim 1.31 \text{ AK}^{-1}\text{m}^{-1}$) [94], and even comparable with multi-layer Fe_nGeTe_2 ($n = 3, 4, 5$) ($0.3\text{--}3.3 \text{ AK}^{-1}\text{m}^{-1}$) [33], sug-

gesting that 2D CrXY is an excellent material platform for thermoelectric applications.

The ATHE, the thermal analogue of AHE, has been widely used to study the charge neutral quasiparticles in quantum materials [95–101]. The calculated ATHC (κ_{xy}) of ML and BL CrXY are plotted in Fig. 12. Similarly to σ_{xy} and α_{xy} , κ_{xy} is vanishing within the band gaps of CrSY and CrSeY. The calculated κ_{xy} at the true Fermi energy for ML (BL) CrTeY with $Y = \text{Cl, Br, and I}$ are 0.02 (0.02) $\text{WK}^{-1}\text{m}^{-1}$, 0.09 (0.07) $\text{WK}^{-1}\text{m}^{-1}$, and 0.12 (0.09) $\text{WK}^{-1}\text{m}^{-1}$, respectively. The ATHE can be further enhanced by doping appropriate holes or electrons. For instance, κ_{xy} increases to its largest value of $0.15 \text{ WK}^{-1}\text{m}^{-1}$ at -0.39 eV for ML CrSBr. In the case of ML (BL) CrTeY, the largest κ_{xy} reaches up to 0.14 (0.11) $\text{WK}^{-1}\text{m}^{-1}$, 0.13 (0.10) $\text{WK}^{-1}\text{m}^{-1}$, and 0.14 (0.17) $\text{WK}^{-1}\text{m}^{-1}$ at -0.37 (-0.34) eV, -0.09 (0.11) eV, and 0.08 (0.13) eV, respectively. The κ_{xy} of 2D CrXY are much larger than that of other vdW ferromagnets, e.g., VI_3 ($0.01 \text{ WK}^{-1}\text{m}^{-1}$) [101].

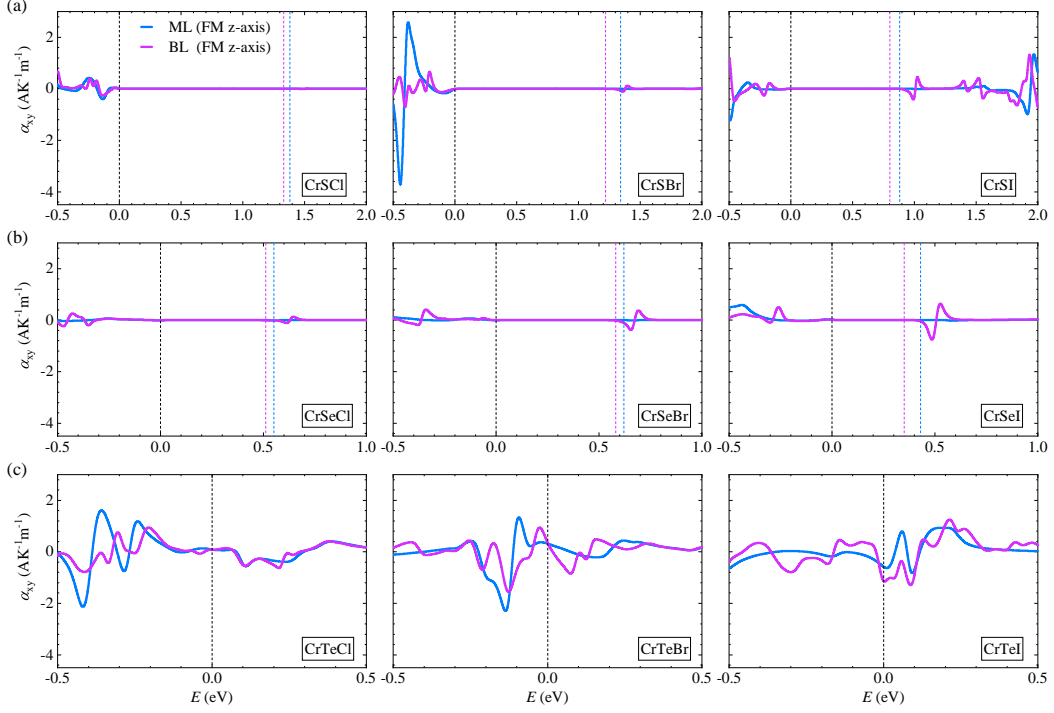


FIG. 11. (Color online) The anomalous Nernst conductivities (α_{xy}) calculated at 100 K as a function of energy for monolayer (blue solid lines) and bilayer (pink solid lines) CrXY with out-of-plane magnetization. The black dashed lines indicate the true Fermi energy for metals or the top of valence bands for semiconductors. The blue and pink dashed lines indicate the bottom of conduction bands for monolayer and bilayer semiconducting CrSY/CrSeY, respectively.

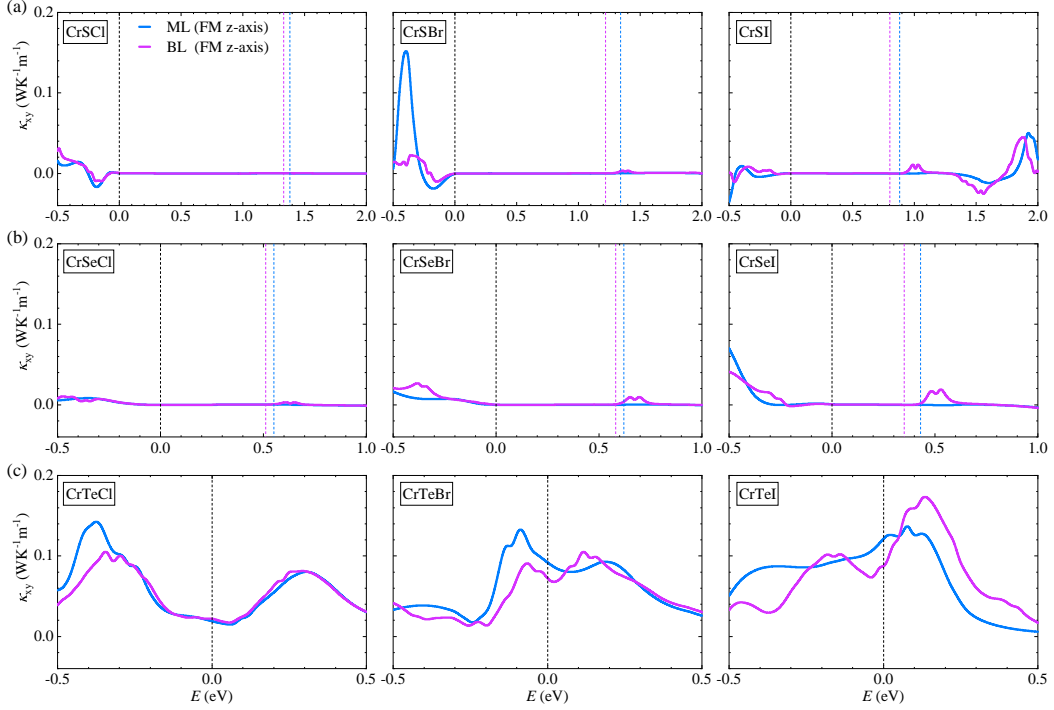


FIG. 12. (Color online) The anomalous thermal Hall conductivities (κ_{xy}) calculated at 100 K as a function of energy for monolayer (blue solid lines) and bilayer (pink solid lines) CrXY with out-of-plane magnetization. The black dashed lines indicate the true Fermi energy for metals or the top of valence bands for semiconductors. The blue and pink dashed lines indicate the bottom of conduction bands for monolayer and bilayer semiconducting CrSY/CrSeY, respectively.

IV. SUMMARY

In summary, we systematically investigated the band structures, magnetocrystalline anisotropy energy, first- and second-order magneto-optical effects, and intrinsically anomalous transport properties in monolayer and bilayer CrXY ($X = \text{S, Se, Te}$; $Y = \text{Cl, Br, I}$) by employing the first-principles calculations. From the band structures, monolayer and bilayer CrSY and CrSeY are identified to be narrow band-gap semiconductors, whereas monolayer and bilayer CrTeY are multi-band metals. The results of magnetocrystalline anisotropy energy show that CrTeBr and CrTeI prefer to out-of-plane magnetization, whereas the other seven family members of CrXY are in favor of in-plane magnetization. The magnetic ground states for bilayer CrXY are confirmed, that is, bilayer CrSI , CrSeCl , and CrTeCl present strong interlayer ferromagnetic coupling, whereas the other ones show interlayer antiferromagnetic coupling. The magnetic group theory identifies the nonzero elements of optical conductivity tensor, which in turn determines the symmetry of magneto-optical Kerr and Faraday effects as well as the anomalous Hall, anomalous Nernst, and anomalous thermal Hall effects. The above physical effects can only exist in monolayer and bilayer ferromagnetic CrXY with out-of-plane magnetization. The magneto-optical strength for the Kerr and Faraday effects of bilayer CrXY are nearly two times that of monolayer CrXY due to the doubled magnetization, and the magneto-optical strength of both monolayer and bilayer CrXY increase distinctly with the increasing of atomic number in X or Y because of the enhanced spin-orbital coupling. The largest Kerr and Faraday rotation angles in the moderate energy range ($1 \sim 5$ eV) are found in bilayer CrSeI , which turns out to be 1.49° and 0.20° , respectively. The anomalous transport properties of CrXY are considerably large under proper hole or electron doping. For instance, the anomalous Hall, anomalous Nernst, and anomalous thermal Hall conductivities reach up to their maximums of

$3.61 e^2/h$, $-3.71 \text{ AK}^{-1}\text{m}^{-1}$, and $0.17 \text{ WK}^{-1}\text{m}^{-1}$ in bilayer CrTeI , monolayer CrSBr , and bilayer CrTeI , respectively. In the case of in-plane magnetization, the second-order magneto-optical effects do exist in both ferromagnetic and antiferromagnetic CrXY , in contrast to the first-order ones. The calculated Schäfer-Hubert and Voigt effects are considerable large in CrXY . For example, the largest Schäfer-Hubert and Voigt rotation angles are found to be 13.39° and -1.67° in bilayer ferromagnetic CrTeCl , and to be 11.31° and -1.50° in bilayer antiferromagnetic CrTeCl , respectively.

Our results show that 2D van der Waals layered magnets CrXY may be excellent material candidates for promising applications to magneto-optical devices, spintronics, and spin caloritronics. For example, the semiconducting CrXY can be used to make van der Waals magnetic heterostructures, similarly to semiconducting ferromagnetic CrI_3 , which realizes the quantum anomalous Hall effect [102] and valley manipulation [103, 104]. The metallic CrXY can also be used to make heterostructures, similarly to metallic Fe_3GeTe_2 , which can increase the critical temperatures of 2D magnetic materials [105], fabricate giant magnetoresistance (GMR) devices [106], design metal electrodes [107], and tailor the anomalous transport properties [108].

ACKNOWLEDGMENTS

The authors thank Gui-Bin Liu, Chaoxi Cui, and Shifeng Qian for their helpful discussion. This work is supported by the National Natural Science Foundation of China (Grant Nos. 11874085, 11734003, and 12061131002), the Sino-German Mobility Programme (Grant No. M-0142), the National Key R&D Program of China (Grant No. 2020YFA0308800), and the Science & Technology Innovation Program of Beijing Institute of Technology (Grant No. 2021CX01020).

-
- [1] N. D. Mermin and H. Wagner, Absence of ferromagnetism or antiferromagnetism in one- or two-dimensional isotropic Heisenberg models, *Phys. Rev. Lett.* **17**, 1133 (1966).
 - [2] B. Huang, G. Clark, E. Navarro-Moratalla, D. R. Klein, R. Cheng, K. L. Seyler, D. Zhong, E. Schmidgall, M. A. McGuire, D. H. Cobden, W. Yao, D. Xiao, P. Jarillo-Herrero, and X. Xu, Layer-dependent ferromagnetism in a van der Waals crystal down to the monolayer limit, *Nature* **546**, 270 (2017).
 - [3] C. Gong, L. Li, Z. Li, H. Ji, A. Stern, Y. Xia, T. Cao, W. Bao, C. Wang, Y. Wang, Z. Q. Qiu, R. J. Cava, S. G. Louie, J. Xia, and X. Zhang, Discovery of intrinsic ferromagnetism in two-dimensional van der Waals crystals, *Nature* **546**, 265 (2017).
 - [4] M. Bonilla, S. Kolekar, Y. Ma, H. C. Diaz, V. Kalappattil, R. Das, T. Eggers, H. R. Gutierrez, M.-H. Phan, and M. Batzill, Strong room-temperature ferromagnetism in VSe_2 monolayers on van der Waals substrates, *Nat. Nanotech.* **13**, 289 (2018).
 - [5] Z.-L. Liu, X. Wu, Y. Shao, J. Qi, Y. Cao, L. Huang, C. Liu, J.-O. Wang, Q. Zheng, Z.-L. Zhu, K. Ibrahim, Y.-L. Wang, and H.-J. Gao, Epitaxially grown monolayer VSe_2 : an air-stable magnetic two-dimensional material with low work function at edges, *Sci. Bull.* **63**, 419 (2018).
 - [6] Z. Fei, B. Huang, P. Malinowski, W. Wang, T. Song, J. Sanchez, W. Yao, D. Xiao, X. Zhu, A. F. May, W. Wu, D. H. Cobden, J.-H. Chu, and X. Xu, Two-dimensional itinerant ferromagnetism in atomically thin Fe_3GeTe_2 , *Nat. Mater.* **17**, 778 (2018).
 - [7] Y. Deng, Y. Yu, Y. Song, J. Zhang, N. Z. Wang, Z. Sun,

- Y. Yi, Y. Z. Wu, S. Wu, J. Zhu, J. Wang, X. H. Chen, and Y. Zhang, Gate-tunable room-temperature ferromagnetism in two-dimensional Fe_3GeTe_2 , *Nature* **563**, 94 (2018).
- [8] X. Zhang, Q. Lu, W. Liu, W. Niu, J. Sun, J. Cook, M. Vaninger, P. F. Miceli, D. J. Singh, S.-W. Lian, T.-R. Chang, X. He, J. Du, L. He, R. Zhang, G. Bian, and Y. Xu, Room-temperature intrinsic ferromagnetism in epitaxial CrTe_2 ultrathin films, *Nat. Commun.* **12**, 2492 (2021).
- [9] H. Katscher and H. Hahn, Über Chalkogenidhalogenide des dreiwertigen Chroms, *Naturwissenschaften* **53**, 361 (1966).
- [10] O. Göser, W. Paul, and H. Kahle, Magnetic properties of CrSBr , *J. Magn. Magn. Mat.* **92**, 129 (1990).
- [11] E. J. Telford, A. H. Dismukes, K. Lee, M. Cheng, A. Wieteska, A. K. Bartholomew, Y.-S. Chen, X. Xu, A. N. Pasupathy, X. Zhu, C. R. Dean, and X. Roy, Layered Antiferromagnetism Induces Large Negative Magnetoresistance in the van der Waals Semiconductor CrSBr , *Adv. Mater.* **32**, 2003240 (2020).
- [12] N. Mounet, M. Gibertini, P. Schwaller, D. Campi, A. Merkys, A. Marrazzo, T. Sohier, I. E. Castelli, A. Cepellotti, G. Pizzi, and N. Marzari, Two-dimensional materials from high-throughput computational exfoliation of experimentally known compounds, *Nat. Nanotech.* **13**, 246 (2018).
- [13] Z. Jiang, P. Wang, J. Xing, X. Jiang, and J. Zhao, Screening and Design of Novel 2D Ferromagnetic Materials with High Curie Temperature above Room Temperature, *ACS Appl. Mater. Interfaces* **10**, 39032 (2018).
- [14] Y. Guo, Y. Zhang, S. Yuan, B. Wang, and J. Wang, Chromium sulfide halide monolayers: intrinsic ferromagnetic semiconductors with large spin polarization and high carrier mobility, *Nanoscale* **10**, 18036 (2018).
- [15] C. Wang, X. Zhou, L. Zhou, N.-H. Tong, Z.-Y. Lu, and W. Ji, A family of high-temperature ferromagnetic monolayers with locked spin-dichroism-mobility anisotropy: MnNX and CrCX ($X = \text{Cl}, \text{Br}, \text{I}; C = \text{S}, \text{Se}, \text{Te}$), *Sci. Bull.* **64**, 293 (2019).
- [16] R. Han, Z. Jiang, and Y. Yan, Prediction of Novel 2D Intrinsic Ferromagnetic Materials with High Curie Temperature and Large Perpendicular Magnetic Anisotropy, *J. Phys. Chem. C* **124**, 7956 (2020).
- [17] H. Wang, J. Qi, and X. Qian, Electrically tunable high Curie temperature two-dimensional ferromagnetism in van der Waals layered crystals, *Appl. Phys. Lett.* **117**, 083102 (2020).
- [18] K. Yang, G. Wang, L. Liu, D. Lu, and H. Wu, Triaxial magnetic anisotropy in the two-dimensional ferromagnetic semiconductor CrSBr , *Phys. Rev. B* **104**, 144416 (2021).
- [19] K. Lee, A. H. Dismukes, E. J. Telford, R. A. Wiscons, J. Wang, X. Xu, C. Nuckolls, C. R. Dean, X. Roy, and X. Zhu, Magnetic Order and Symmetry in the 2D Semiconductor CrSBr , *Nano Lett.* **21**, 3511 (2021).
- [20] N. P. Wilson, K. Lee, J. Cenker, K. Xie, A. H. Dismukes, E. J. Telford, J. Fonseca, S. Sivakumar, C. Dean, T. Cao, X. Roy, X. Xu, and X. Zhu, Interlayer electronic coupling on demand in a 2D magnetic semiconductor, *Nat. Mater.* **20**, 1657 (2021).
- [21] E. J. Telford, A. H. Dismukes, R. L. Dudley, R. A. Wiscons, K. Lee, J. Yu, S. Shabani, A. Scheie, K. Watanabe, T. Taniguchi, D. Xiao, A. N. Pasupathy, C. Nuckolls, X. Zhu, C. R. Dean, and X. Roy, Hidden low-temperature magnetic order revealed through magnetotransport in monolayer CrSBr , [arXiv:2106.08471](https://arxiv.org/abs/2106.08471).
- [22] D. J. Rizzo, A. S. McLeod, C. Carnahan, E. J. Telford, A. H. Dismukes, R. A. Wiscons, Y. Dong, C. Nuckolls, C. R. Dean, A. N. Pasupathy, X. Roy, D. Xiao, and D. N. Basov, Visualizing Atomically Layered Magnetism in CrSBr , *Adv. Mater.* **34**, 2201000 (2022).
- [23] J. Cenker, S. Sivakumar, K. Xie, A. Miller, P. Thijssen, Z. Liu, A. Dismukes, J. Fonseca, E. Anderson, X. Zhu, X. Roy, D. Xiao, J.-H. Chu, T. Cao, and X. Xu, Reversible strain-induced magnetic phase transition in a van der Waals magnet, *Nat. Nanotech.* **17**, 256 (2022).
- [24] Y. J. Bae, J. Wang, J. Xu, D. G. Chica, G. M. Diederich, J. Cenker, M. E. Ziebel, Y. Bai, H. Ren, C. R. Dean, M. Delor, X. Xu, X. Roy, A. D. Kent, and X. Zhu, Exciton-Coupled Coherent Antiferromagnetic Magnons in a 2D Semiconductor, [arXiv:2201.13197](https://arxiv.org/abs/2201.13197).
- [25] T. S. Ghiasi, A. A. Kaverzin, A. H. Dismukes, D. K. de Wal, X. Roy, and B. J. van Wees, Electrical and thermal generation of spin currents by magnetic bilayer graphene, *Nat. Nanotech.* **16**, 788 (2021).
- [26] J. K. LL.D., On rotation of the plane of polarization by reflection from the pole of a magnet, *Phil. Mag.* **3**, 321 (1877).
- [27] M. Faraday, Experimental researches in electricity.-Nineteenth series, *Phil. Trans. R. Soc.* **136**, 1 (1846).
- [28] R. Schäfer and A. Hubert, A new magneto-optic effect related to non-uniform magnetization on the surface of a ferromagnet, *phys. stat. sol. (a)* **118**, 271 (1990).
- [29] W. Voigt, Magneto-und elektrooptik, 3 (BG Teubner, 1908).
- [30] N. Nagaosa, J. Sinova, S. Onoda, A. H. MacDonald, and N. P. Ong, Anomalous hall effect, *Rev. Mod. Phys.* **82**, 1539 (2010).
- [31] W. Nernst, Ueber die electromotorischen Kräfte, welche durch den Magnetismus in von einem Wärmestrome durchflossenen Metallplatten geweckt werden, *Ann. Phys.* **267**, 760 (1887).
- [32] T. Qin, Q. Niu, and J. Shi, Energy Magnetization and the Thermal Hall Effect, *Phys. Rev. Lett.* **107**, 236601 (2011).
- [33] X. Yang, X. Zhou, W. Feng, and Y. Yao, Strong magneto-optical effect and anomalous transport in the two-dimensional van der Waals magnets Fe_nGeTe_2 ($n = 3, 4, 5$), *Phys. Rev. B* **104**, 104427 (2021).
- [34] Y. Suzuki, T. Katayama, S. Yoshida, K. Tanaka, and K. Sato, New magneto-optical transition in ultrathin $\text{Fe}(100)$ films, *Phys. Rev. Lett.* **68**, 3355 (1992).
- [35] G. Y. Guo and H. Ebert, Band-theoretical investigation of the magneto-optical Kerr effect in Fe and Co multilayers, *Phys. Rev. B* **51**, 12633 (1995).
- [36] P. Ravindran, A. Delin, P. James, B. Johansson, J. M. Wills, R. Ahuja, and O. Eriksson, Magnetic, optical, and magneto-optical properties of MnX ($X = \text{As}, \text{Sb}, \text{or Bi}$) from full-potential calculations, *Phys. Rev. B* **59**, 15680 (1999).
- [37] G. Ghosh, Dispersion-equation coefficients for the refractive index and birefringence of calcite and quartz crystals, *Opt. Commun.* **163**, 95 (1999).
- [38] An online database of refractive index, <https://refractiveindex.info/>.
- [39] N. Tesařová, T. Ostatnický, V. Novák, K. Olejník,

- J. Šubrt, H. Reichlová, C. T. Ellis, A. Mukherjee, J. Lee, G. M. Sipahi, J. Sinova, J. Hamrle, T. Jungwirth, P. Němec, J. Černe, and K. Výborný, Systematic study of magnetic linear dichroism and birefringence in (Ga,Mn)As, *Phys. Rev. B* **89**, 085203 (2014).
- [40] H.-C. Mertins, P. M. Oppeneer, J. Kuneš, A. Gaupp, D. Abramsohn, and F. Schäfers, Observation of the X-Ray Magneto-Optical Voigt Effect, *Phys. Rev. Lett.* **87**, 047401 (2001).
- [41] A. A. Mostofi, J. R. Yates, Y.-S. Lee, I. Souza, D. Vanderbilt, and N. Marzari, wannier90: A tool for obtaining maximally-localised Wannier functions, *Comput. Phys. Commun.* **178**, 685 (2008).
- [42] J. R. Yates, X. Wang, D. Vanderbilt, and I. Souza, Spectral and Fermi surface properties from Wannier interpolation, *Phys. Rev. B* **75**, 195121 (2007).
- [43] J. H. Strait, P. Nene, and F. Rana, High intrinsic mobility and ultrafast carrier dynamics in multilayer metal-dichalcogenide MoS₂, *Phys. Rev. B* **90**, 245402 (2014).
- [44] N. Sivadas, S. Okamoto, and D. Xiao, Gate-Controllable Magneto-optic Kerr Effect in Layered Collinear Antiferromagnets, *Phys. Rev. Lett.* **117**, 267203 (2016).
- [45] See Supplemental Material at <http://link.aps.org/xxx>, which includes convergence test, structural information, and supplementary data and figures.
- [46] Y. Yao, L. Kleinman, A. H. MacDonald, J. Sinova, T. Jungwirth, D.-s. Wang, E. Wang, and Q. Niu, First principles calculation of anomalous Hall conductivity in ferromagnetic bcc Fe, *Phys. Rev. Lett.* **92**, 037204 (2004).
- [47] N. W. Ashcroft and N. D. Mermin, Solid state physics (SaundersCollege Publishing, Philadelphia, 1976).
- [48] H. van Houten, L. W. Molenkamp, C. W. J. Beenakker, and C. T. Foxon, Thermo-electric properties of quantum point contacts, *Semicond. Sci. Technol.* **7**, B215 (1992).
- [49] K. Behnia, Fundamentals of thermoelectricity (Oxford University Press, 2015).
- [50] G. Kresse and J. Hafner, Ab initio molecular dynamics for liquid metals, *Phys. Rev. B* **47**, 558 (1993).
- [51] G. Kresse and J. Furthmüller, Efficient iterative schemes for ab initio total-energy calculations using a plane-wave basis set, *Phys. Rev. B* **54**, 11169 (1996).
- [52] P. E. Blöchl, Projector augmented-wave method, *Phys. Rev. B* **50**, 17953 (1994).
- [53] J. P. Perdew, K. Burke, and M. Ernzerhof, Generalized gradient approximation made simple, *Phys. Rev. Lett.* **77**, 3865 (1996).
- [54] J. Klimeš, D. R. Bowler, and A. Michaelides, Chemical accuracy for the van der Waals density functional, *J. Phys.: Condens. Matter* **22**, 022201 (2009).
- [55] K. Lee, E. D. Murray, L. Kong, B. I. Lundqvist, and D. C. Langreth, Higher-accuracy van der Waals density functional, *Phys. Rev. B* **82**, 081101 (2010).
- [56] J. Klimeš, D. R. Bowler, and A. Michaelides, Van der Waals density functionals applied to solids, *Phys. Rev. B* **83**, 195131 (2011).
- [57] A. I. Liechtenstein, V. I. Anisimov, and J. Zaanen, Density-functional theory and strong interactions: Orbital ordering in Mott-Hubbard insulators, *Phys. Rev. B* **52**, R5467 (1995).
- [58] T. Woźniak, P. E. Faria Junior, G. Seifert, A. Chaves, and J. Kunstmann, Exciton g factors of van der Waals heterostructures from first-principles calculations, *Phys. Rev. B* **101**, 235408 (2020).
- [59] T. Deilmann, P. Krüger, and M. Rohlfing, Ab Initio Studies of Exciton g Factors: Monolayer Transition Metal Dichalcogenides in Magnetic Fields, *Phys. Rev. Lett.* **124**, 226402 (2020).
- [60] J. Förste, N. V. Tepliakov, S. Y. Kruchinin, J. Lindlau, M. F. Victor Funk, K. Watanabe, T. Taniguchi, A. S. Baimuratov, and A. Högele, Exciton g -factors in monolayer and bilayer WSe₂ from experiment and theory, *Nat. Commun.* **11**, 4539 (2020).
- [61] F. Xuan and S. Y. Quek, Valley Zeeman effect and Landau levels in two-dimensional transition metal dichalcogenides, *Phys. Rev. Research* **2**, 033256 (2020).
- [62] H. T. Stokes, D. M. Hatch, and B. J. Campbell, ISOTROPY Software Suite., <https://stokes.byu.edu/iso/isotropy.php>.
- [63] J. Klein, T. Pham, J. D. Thomsen, J. B. Curtis, M. Lorke, M. Florian, A. Steinhoff, R. A. Wiscons, J. Luxa, Z. Sofer, F. Jahnke, P. Narang, and F. M. Ross, Atomistic spin textures on-demand in the van der Waals layered magnet CrSBr, [arXiv:2107.00037](https://arxiv.org/abs/2107.00037).
- [64] P. W. Anderson, Antiferromagnetism. Theory of Superexchange Interaction, *Phys. Rev.* **79**, 350 (1950).
- [65] J. B. Goodenough, An interpretation of the magnetic properties of the perovskite-type mixed crystals La_{1-x}Sr_xCoO_{3-λ}, *J. Phys. Chem. Solids* **6**, 287 (1958).
- [66] J. Kanamori, Superexchange interaction and symmetry properties of electron orbitals, *J. Phys. Chem. Solids* **10**, 87 (1959).
- [67] H. H. Kim, B. Yang, S. Li, S. Jiang, C. Jin, Z. Tao, G. Nichols, F. Sfigakis, S. Zhong, C. Li, S. Tian, D. G. Cory, G.-X. Miao, J. Shan, K. F. Mak, H. Lei, K. Sun, L. Zhao, and A. W. Tsen, Evolution of interlayer and intralayer magnetism in three atomically thin chromium trihalides, *Proc. Natl. Acad. Sci. USA* **116**, 11131 (2019).
- [68] X. Zhou, J.-P. Hanke, W. Feng, F. Li, G.-Y. Guo, Y. Yao, S. Blügel, and Y. Mokrousov, Spin-order dependent anomalous Hall effect and magneto-optical effect in the noncollinear antiferromagnets Mn₃XN with X = Ga, Zn, Ag, or Ni, *Phys. Rev. B* **99**, 104428 (2019).
- [69] M. Wu, Z. Li, T. Cao, and S. G. Louie, Physical origin of giant excitonic and magneto-optical responses in two-dimensional ferromagnetic insulators, *Nat. Commun.* **10**, 2371 (2020).
- [70] A. Molina-Sánchez, G. Catarina, D. Sangalli, and J. Fernández-Rossier, Magneto-optical response of chromium trihalide monolayers: chemical trends, *J. Mater. Chem. C* **8**, 8856 (2020).
- [71] V. K. Gudelli and G.-Y. Guo, Magnetism and magneto-optical effects in bulk and few-layer CrI₃: a theoretical GGA + U study, *New J. Phys.* **21**, 053012 (2019).
- [72] X. Yang, X. Zhou, W. Feng, and Y. Yao, Tunable magneto-optical effect, anomalous Hall effect, and anomalous Nernst effect in the two-dimensional room-temperature ferromagnet 1T-CrTe₂, *Phys. Rev. B* **103**, 024436 (2021).
- [73] Y. Fang, S. Wu, Z.-Z. Zhu, and G.-Y. Guo, Large magneto-optical effects and magnetic anisotropy energy in two-dimensional Cr₂Ge₂Te₆, *Phys. Rev. B* **98**, 125416 (2018).
- [74] X. Zhou, W. Feng, F. Li, and Y. Yao, Large magneto-optical effects in hole-doped blue phosphorene and gray arsenene, *Nanoscale* **9**, 17405 (2017).

- [75] W. Feng, G.-Y. Guo, and Y. Yao, Tunable magneto-optical effects in hole-doped group-IIIA metal-monochalcogenide monolayers, *2D Mater.* **4**, 015017 (2017).
- [76] Z. Zheng, J. Y. Shi, Q. Li, T. Gu, H. Xia, L. Q. Shen, F. Jin, H. C. Yuan, Y. Z. Wu, L. Y. Chen, and H. B. Zhao, Magneto-optical probe of ultrafast spin dynamics in antiferromagnetic CoO thin films, *Phys. Rev. B* **98**, 134409 (2018).
- [77] V. Saidl, P. Němec, P. Wadley, V. Hills, R. P. Campion, V. Novák, K. W. Edmonds, F. Maccherozzi, S. S. Dhesi, B. L. Gallagher, F. Trojánek, J. Kuneš, J. Železný, P. Malý, and T. Jungwirth, Optical determination of the Néel vector in a CuMnAs thin-film antiferromagnet, *Nat. Photon.* **11**, 91 (2017).
- [78] V. Antonov, B. Harmon, and A. Yaresko, Electronic structure and magneto-optical properties of solids (Springer Science & Business Media, 2004).
- [79] P. M. Oppeneer, T. Maurer, J. Sticht, and J. Kübler, Ab initio calculated magneto-optical Kerr effect of ferromagnetic metals: Fe and Ni, *Phys. Rev. B* **45**, 10924 (1992).
- [80] W. Feng, J.-P. Hanke, X. Zhou, G.-Y. Guo, S. Blügel, Y. Mokrousov, and Y. Yao, Topological magneto-optical effects and their quantization in noncoplanar antiferromagnets, *Nat. Commun.* **11**, 118 (2020).
- [81] X. Zhou, W. Feng, X. Yang, G.-Y. Guo, and Y. Yao, Crystal chirality magneto-optical effects in collinear antiferromagnets, *Phys. Rev. B* **104**, 024401 (2021).
- [82] E. Oh, D. U. Bartholomew, A. K. Ramdas, J. K. Furdyna, and U. Debska, Voigt effect in diluted magnetic semiconductors: $\text{Cd}_{1-x}\text{Mn}_x\text{Te}$ and $\text{Cd}_{1-x}\text{Mn}_x\text{Se}$, *Phys. Rev. B* **44**, 10551 (1991).
- [83] A. Ramasubramaniam and D. Naveh, Mn-doped monolayer MoS_2 : An atomically thin dilute magnetic semiconductor, *Phys. Rev. B* **87**, 195201 (2013).
- [84] L. Sun, W. Zhou, Y. Liang, L. Liu, and P. Wu, Magnetic properties in Fe-doped SnS_2 : Density functional calculations, *Comput. Mater. Sci.* **117**, 489 (2016).
- [85] L. J. Li, E. C. T. O'Farrell, K. P. Loh, G. Eda, B. Özyilmaz, and A. H. C. Neto, Controlling many-body states by the electric-field effect in a two-dimensional material, *Nature* **529**, 185 (2016).
- [86] K. Kim, J. Seo, E. Lee, K.-T. Ko, B. S. Kim, B. G. Jang, J. M. Ok, J. Lee, Y. J. Jo, W. Kang, J. H. Shim, C. Kim, H. W. Yeom, B. I. Min, B.-J. Yang, and J. S. Kim, Large anomalous Hall current induced by topological nodal lines in a ferromagnetic van der Waals semimetal, *Nat. Mater.* **17**, 794 (2018).
- [87] J. Xu, W. A. Phelan, and C.-L. Chien, Large Anomalous Nernst Effect in a van der Waals Ferromagnet Fe_3GeTe_2 , *Nano Lett.* **19**, 8250 (2019).
- [88] J. Seo, D. Y. Kim, E. S. An, K. Kim, G.-Y. Kim, S.-Y. Hwang, D. W. Kim, B. G. Jang, H. Kim, G. Eom, S. Y. Seo, R. Stania, M. Muntwiler, J. Lee, K. Watanabe, T. Taniguchi, Y. J. Jo, J. Lee, B. I. Min, M. H. Jo, H. W. Yeom, S.-Y. Choi, J. H. Shim, and J. S. Kim, Nearly room temperature ferromagnetism in a magnetic metal-rich van der Waals metal, *Sci. Adv.* **6**, eaay8912 (2020).
- [89] P. N. Dheer, Galvanomagnetic Effects in Iron Whiskers, *Phys. Rev.* **156**, 637 (1967).
- [90] G. E. W. Bauer, E. Saitoh, and B. J. van Wees, Spin caloritronics, *Nat. Mater.* **11**, 391 (2012).
- [91] S. R. Boona, R. C. Myers, and J. P. Heremans, Spin caloritronics, *Energy Environ. Sci.* **7**, 885 (2014).
- [92] D. Xiao, Y. Yao, Z. Fang, and Q. Niu, Berry-phase effect in anomalous thermoelectric transport, *Phys. Rev. Lett.* **97**, 026603 (2006).
- [93] S. N. Guin, P. Vir, Y. Zhang, N. Kumar, S. J. Watzman, C. Fu, E. Liu, K. Manna, W. Schnelle, J. Gooth, C. Shekhar, Y. Sun, and C. Felser, Zero-Field Nernst Effect in a Ferromagnetic Kagome-Lattice Weyl-Semimetal $\text{Co}_3\text{Sn}_2\text{S}_2$, *Adv. Mater.* **31**, 1806622 (2019).
- [94] J. Noky, J. Gayles, C. Felser, and Y. Sun, Strong anomalous Nernst effect in collinear magnetic Weyl semimetals without net magnetic moments, *Phys. Rev. B* **97**, 220405 (2018).
- [95] Y. Onose, T. Ideue, H. Katsura, Y. Shiomi, N. Nagaosa, and Y. Tokura, Observation of the Magnon Hall Effect, *Science* **329**, 297 (2010).
- [96] M. Hirschberger, J. W. Krizan, R. J. Cava, and N. P. Ong, Large thermal Hall conductivity of neutral spin excitations in a frustrated quantum magnet, *Science* **348**, 106 (2015).
- [97] M. Hirschberger, R. Chisnell, Y. S. Lee, and N. P. Ong, Thermal Hall Effect of Spin Excitations in a Kagome Magnet, *Phys. Rev. Lett.* **115**, 106603 (2015).
- [98] H. Doki, M. Akazawa, H.-Y. Lee, J. H. Han, K. Sugii, M. Shimozawa, N. Kawashima, M. Oda, H. Yoshida, and M. Yamashita, Spin Thermal Hall Conductivity of a Kagome Antiferromagnet, *Phys. Rev. Lett.* **121**, 097203 (2018).
- [99] K. Sugii, M. Shimozawa, D. Watanabe, Y. Suzuki, M. Halim, M. Kimata, Y. Matsumoto, S. Nakatsuji, and M. Yamashita, Thermal Hall Effect in a Phonon-Glass $\text{Ba}_3\text{CuSb}_2\text{O}_9$, *Phys. Rev. Lett.* **118**, 145902 (2017).
- [100] M. Akazawa, M. Shimozawa, S. Kittaka, T. Sakakibara, R. Okuma, Z. Hiroi, H.-Y. Lee, N. Kawashima, J. H. Han, and M. Yamashita, Thermal Hall Effects of Spins and Phonons in Kagome Antiferromagnet Cd-Kapellasite, *Phys. Rev. X* **10**, 041059 (2020).
- [101] H. Zhang, C. Xu, C. Carnahan, M. Sretenovic, N. Suri, D. Xiao, and X. Ke, Anomalous Thermal Hall Effect in an Insulating van der Waals Magnet, *Phys. Rev. Lett.* **127**, 247202 (2021).
- [102] J. Zhang, B. Zhao, T. Zhou, Y. Xue, C. Ma, and Z. Yang, Strong magnetization and Chern insulators in compressed graphene/ CrI_3 van der Waals heterostructures, *Phys. Rev. B* **97**, 085401 (2018).
- [103] D. Zhong, K. L. Seyler, X. Linpeng, R. Cheng, N. Sivadas, B. Huang, E. Schmidgall, T. Taniguchi, K. Watanabe, M. A. McGuire, W. Yao, D. Xiao, K.-M. C. Fu, and X. Xu, Van der Waals engineering of ferromagnetic semiconductor heterostructures for spin and valleytronics, *Sci. Adv.* **3**, e1603113 (2017).
- [104] K. L. Seyler, D. Zhong, B. Huang, X. Linpeng, N. P. Wilson, T. Taniguchi, K. Watanabe, W. Yao, D. Xiao, M. A. McGuire, K.-M. C. Fu, and X. Xu, Valley Manipulation by Optically Tuning the Magnetic Proximity Effect in $\text{WSe}_2/\text{CrI}_3$ Heterostructures, *Nano Lett.* **18**, 3823 (2018).
- [105] H. Wang, Y. Liu, P. Wu, W. Hou, Y. Jiang, X. Li, C. Pandey, D. Chen, Q. Yang, H. Wang, D. Wei, N. Lei, W. Kang, L. Wen, T. Nie, W. Zhao, and K. L. Wang, Above Room-Temperature Ferromagnetism in Wafer-Scale Two-Dimensional van der Waals Fe_3GeTe_2 Tai-

- lored by a Topological Insulator, [ACS Nano](#) **14**, 10045 (2020).
- [106] S. Albarakati, C. Tan, Z.-J. Chen, J. G. Partridge, G. Zheng, L. Farrar, E. L. H. Mayes, M. R. Field, C. Lee, Y. Wang, Y. Xiong, M. Tian, F. Xiang, A. R. Hamilton, O. A. Tretiakov, D. Culcer, Y.-J. Zhao, and L. Wang, Antisymmetric magnetoresistance in van der Waals $\text{Fe}_3\text{GeTe}_2/\text{graphite}/\text{Fe}_3\text{GeTe}_2$ trilayer heterostructures, [Sci. Adv.](#) **5**, eaaw0409 (2019).
- [107] Q. Wu, Y. S. Ang, L. Cao, and L. K. Ang, Design of metal contacts for monolayer Fe_3GeTe_2 based devices, [Appl. Phys. Lett.](#) **115**, 083105 (2019).
- [108] Y. Shao, W. Lv, J. Guo, B. Qi, W. Lv, S. Li, G. Guo, and Z. Zeng, The current modulation of anomalous Hall effect in van der Waals $\text{Fe}_3\text{GeTe}_2/\text{WTe}_2$ heterostructures, [Appl. Phys. Lett.](#) **116**, 092401 (2020).